Classical and Quantum Spin Pumps

Disertación para optar al título de
Doctor en Ciencias-Física de la
Universidad Nacional de Colombia

por

Fredy Leonardo Dubeibe Marín

Bogotá, Junio de 2010

Classical and Quantum Spin Pumps

Fredy Leonardo Dubeibe Marín
Código 183154

Disertación para optar al título de
Doctor en Ciencias-Física de la
Universidad Nacional de Colombia

Dirigido por
Prof. Thomas Dittrich

Universidad Nacional de Colombia
Facultad de Ciencias
Departamento de Física
Bogotá, Junio de 2010

Abstract

Directed transport in classical and quantum pumps is studied in a specific model, a magnetic dipole moving in a periodically modulated magnetic field confined to a compact region in space. For the classical case, we show that this system is an irregular scatterer in large parts of its parameter space. If all spatio-temporal symmetries are broken, directed transport of mass as well as angular momentum occurs. The sensitive parameter dependence of the corresponding currents includes frequent sign reversals. Zeros of either current quantity correspond to the exclusive occurrence of the other and thus give rise in particular to angular-momentum separation without mass transport as a classical analogue of spin-polarized currents. For the quantum case, we show that the basic mechanism responsible for the separation of spins in the classical case carries over to the quantum level, giving rise to a spin pump capable of generating polarized spin currents. We illustrate and confirm our theory with numerical data obtained from wave packet scattering as well as from a numerical solution of the Schrödinger equation with source term, and show how the scattering parameters for individual Floquet channels are extracted from the raw data.

"In life, time is the solution to almost all the problems.
In physics, time is the problem to almost all the solutions."

Acknowledgments

I would like to thank all people who have helped and inspired me during my doctoral study.

I specially want to thank my advisor, Prof. Thomas Dittrich for his invaluable help and support over the whole period of my PhD studies. Above all and the most needed, he provided me unflinching encouragement and support in various ways. His truly scientist intuition, ideas and passion for science, exceptionally inspire and enrich my growth as a student, researcher and scientist I want to be. I am indebted to him more than he knows.

I would like here to express my deep and sincere gratitude to everyone of the members of the group Caos y Complejidad in Colombia, who made it a convivial place to work. In particular, I would like to thank Leonardo and Ivonne for his friendship and help in the past years. They and all other folks, had inspired me in research and life through our interactions during the long hours in the 802. Thanks.

My deepest gratitude goes to my parents for their unflagging love and support throughout my life. I am indebted to my mother, Doña Nelly, for his care and love. As a typical mother in a Colombian family, she worked hardly to help supporting the family, and spare no effort to provide the best possible environment for me and my siblings to grow up and attend school. She had never complained in spite of all the hardships in her life. Mother, I love you. I want to thank to my father, Don Dumar, it is thanks to him that I first became interested in science when I was a child. His encourage for discover, understand and invention, always oriented me towards physics. Although our ideas about almost everything are now widely divergent, thank you.

I am specially thankful to my son, Juanda, for being the primary motivation to start and finish this project. I am grateful for his patience and for the many mature discussions we shared. In this world, there is nothing more important than you. I couldn't have a better son and I don't know how to put in words how much I love you. This thesis is dedicated to you chiquitín.

Finally, the Complex Quantum Systems group in Regensburg has treated me very kindly the time I've spent there. Tobias, Boris, Juan Diego and Jürgen helped me with all kind of things they didn't have to help me with. A research group is no more and no less than the

people that belong to it. At the Quantum Complex Systems group every one joins to create a constructive and friendly atmosphere. An ideal atmosphere for doing science. I owe my most sincere gratitude to Professor Klaus Richter, who gave me the opportunity to work with them in the Physics Department at the University of Regensburg, in Regensburg Germany, and gave me untiring help during my stay in Germany. His wide knowledge and his logical way of thinking have been of great value for me. Danke!

The financial support of the DAAD - Deutscher Akademischer Austausch Dienst, VolkswagenStiftung, Colciencias and PBESP - Programa de Becas para Estudiantes Sobresalientes de Posgrado at the Universidad Nacional is gratefully acknowledged.

Contents

Abstract ii

1 Introduction 1

2 Classical Angular Momentum Pump 5
2.1 Classical Model . . . 5
2.1.1 Basic setup: Coupling internal to external freedoms . . . 5
2.1.2 Equations of motion . . . 6
2.1.3 Symmetry considerations . . . 8
2.1.4 Discrete-time dynamics . . . 9
2.1.5 Time scales . . . 10
2.2 Chaotic scattering . . . 10
2.2.1 Deflection functions . . . 11
2.2.2 Stable and unstable periodic orbits . . . 13
2.2.3 Delay-time statistics . . . 15
2.3 Directed transport . . . 15
2.3.1 Asymmetric scattering and directed currents . . . 16
2.3.2 Angular-momentum transport . . . 19
2.4 Summary . . . 19

3 Wave–Packet Evolution 21
3.1 The Method . . . 21
3.1.1 Inverse of a Tridiagonal Matrix . . . 24
3.1.2 Particle Scattered from a Finite Square Potential Well . . . 25
3.1.3 Particle Scattered from a Finite Square barrier . . . 26
3.2 Method with Absorbing Boundary Conditions . . . 27
3.2.1 Particle Scattered from a Finite Square Potential Well . . . 31
3.2.2 Particle Scattered from a Finite Square barrier . . . 32

3.3 Method with Absorbing Boundary Conditions and Source Term 33
3.3.1 Plane Waves with Constant Amplitude 34
3.3.2 Plane Waves with Time–Dependent Amplitude 35
3.4 Summary 36

4 Quantum Spin Pump **38**
4.1 The Floquet Operator 38
4.1.1 Numerical Evaluation of the Propagator in the Position Representation 40
4.1.2 Numerical Evaluation of the Propagator using Finite Differences . . . 41
4.2 The Floquet Operator for Decoupled Spinors 42
4.2.1 Comparison of the Numerical Methods 44
4.2.2 Floquet Channels 46
4.3 The Floquet Operator for Coupled Spinors 49
4.3.1 Directed Transport 51
4.4 Summary 53

5 Conclusions **54**

A Neutral Particle in an Inhomogeneous Magnetic Field **56**

B Particle Current **59**

C Spin Current **61**

List of Tables

4.1 Transmission coefficients using Finite Differences and the Floquet operator . 45

List of Figures

2.1 Schematic representation of the scattering process involving the spin vector . 7
2.2 Configuration of the magnetic fields 8
2.3 The phase ϕ_{in} of a scattering trajectory 9
2.4 Deflection functions vs. initial phase 11
2.5 Deflection functions vs. initial polar angle 12
2.6 Periodic orbit for a map and Poincaré map for a vector field 13
2.7 Examples of an unstable and a stable periodic orbit 14
2.8 Poincaré sections in the (x, p)-plane 14
2.9 Delay-time statistics 16
2.10 Qualitative outcome of scattering 17
2.11 Effective outgoing spin with and without spatial symmetry 17
2.12 Effective outgoing spin as a function of the width and amplitude 18
2.13 Finite spin current in absence of net mass (charge) transport 19
2.14 Particle current and spin current vs. the width of the well 20
2.15 Particle current and spin current vs. the field strength 20

3.1 Particle scattered from a finite square potential well without ABC 26
3.2 Particle scattered from a finite square barrier without ABC 27
3.3 Dispersion relation and its first order approximation 29
3.4 Particle scattered from a finite square potential well with ABC 32
3.5 Particle scattered from a finite square barrier with ABC 33
3.6 Solutions of the Schrödinger equation with source term 35
3.7 Solutions of the Schrödinger equation with time–dependent source term . . . 36
3.8 Probability density for the case of a time–dependent source term 37

4.1 Probability density for the evolution of a free wave packet 45
4.2 Transmission and reflection coefficients vs. the period of the kicks 46
4.3 Allowed integers for the discretized momentum vs. the Floquet channels . . . 47

4.4 Wave packets in momentum and position representation 48
4.5 Evolution operator in position representation for decoupled spinors 48
4.6 Graphics of the different kinds of interaction in the whole numerical region. . 50
4.7 Time-evolution of the probability density for an initial spin-up state 52
4.8 Evolution operator in position representation for coupled spinors 52
4.9 Comparison of particle current to spin current for coupled spinors 53

1 Introduction

Electronics is based on the principle of generating or controlling electrical currents by exploiting the charge nature of electrons, that is manipulating the motion of the charge carrier through their interaction with external electric or electromagnetic fields. Spintronics [1] or spin electronics, follows the vision to employ another intrinsic feature of electrons, namely that they carry a spin. Usually electrons are unpolarized: their spins do not have a preferred direction. Using the spin nature of electrons is desirable to prepare electrons in defined spin states, e.g. spin-up or spin-down states with respect to a certain (field) direction. This could be achieved, for example, using magnetic metals, magnetic semiconductors or spin pumps.

In the case of magnetic materials, it has been demonstrated that the combined effect of a spatially periodic potential, lateral confinement and spin-orbit interaction gives rise to a quantum ratchet mechanism for spin-polarized currents in two-dimensional coherent conductors. Upon adiabatic ac-driving, in the absence of a static bias, the system generates a directed spin current [2]. On the other hand, a parametric quantum pump generates a dc electric current by a cyclic variation of pumping potentials inside the scattering system while keeping the leads at a constant chemical potential (see e.g. [3] and references therein). There has been found that the pumped current is rather sensitive to various parameters of the system such as the potential landscape of the pump, the frequency of the driving force, the Fermi energy of the leads, and the energy of the central scattering regime [4]. As parameters vary, the pumped current can be spin-polarized [5], which results in generating of the spin current.

Despite the methods previously cited in most of the cases have well established results, should be pointed out, that the quantum dynamics simulations are also important to provide a detailed description of a phenomenon in terms of the underlying nature of the system. This could be archived in some cases, by solving the time-dependent Schrödinger equation variationally using a straightforward basis-set expansion of the wave function, which is known as wave packet dynamics. Wave-packet propagation methods are particularly attractive: they are simple to implement, and provide easily observable results of the evolving system that can be related to experiment. The most powerful wave-packet dynamics algorithm at present, able to treat larger systems than the standard methods, is multi-configurational time-dependent

Hartree (MCTDH) [6], however this algorithm is very cumbersome to use in practice.

Here we propose a model based on directed transport phenomena in systems with chaotic scattering. We first construct the classical model and study its peculiarities and afterwards its quantum mechanical consequences. Concerning the classical framework, in this thesis we present a case study of chaotic scattering with an internal degree of freedom, intrinsic angular momentum, and consider how it contributes to irregular scattering and how in turn directed transport of this quantity arises from scattering. The subject bears on various of the research lines: we shall invoke much of what is known about chaotic scattering, in particular in periodically driven systems [7, 8]. The coupling of a magnetic dipole to an inhomogeneous magnetic field [9] is crucial for our modeling. Also concerning chaotic dynamics in such a configuration we refer to earlier work [10]; in fact, it is the essential ingredient of one of the first models proposed for irregular scattering [11].

In directed transport, we take all the insights into account that concern the importance of binary spatio-temporal symmetries and their breaking [12, 13, 14, 15]. We here can fall back on direct precursor work on chaotic pumps [16]. The definition of spin current is adopted from quantum contexts to define angular-momentum transport in a classical setting. It should be emphasized, that we consider a driving that is both strong and fast [7, 8] and thus incompatible with any perturbative and/or adiabatic approximation. In this sense, we are dealing with strongly nonlinear transport phenomena, far off the regime of linear response and in particular of peristaltic pumping [17, 18, 19, 20]. As a consequence, directed transport is achieved already driving the system via a *single* parameter, albeit with a profile asymmetric under time reversal. The crucial rôle of chaos also distinguishes our work from recent studies of spin ratchets in ballistic electron systems [21, 22, 23].

Here we present conclusive evidence that in classical chaotic scattering systems, polarized currents can be generated, i.e., directed transport of angular momentum occurs independently and even in the absence of mass (charge) transport. We explain this effect in terms of the interplay of asymmetry and the randomizing action of long unstable trajectories, thus corroborating the decisive rôle of chaotic scattering. It is also manifest in the sensitive parameter dependence of mass as well as angular-momentum currents, which allows for a fine tuning of both quantities. In particular, sign reversals are frequent and zeros of one current give rise to the exclusive dominance of the other. In this way, we achieve a "rectification of angular momentum" in the absence of mass transport [24, 25].

Concerning the quantum-mechanical scattering process, here we implement a numerical integration scheme, in order to study the time-dependent dynamics in the scatterer. First, we formulate the problem in terms of Gaussian wave packets impinging the scattering region and being reflected or transmitted. Wave packets (WP) are a very useful concept when analyzing quantum-mechanical scattering processes, since they combine local and wavelike aspects on an equal footing. Some of their more recent applications range from studies of the intrinsic spin Hall effect in semiconductors [26], spin-flip dynamics [27], thermal averaging, and its influence on interference patterns [28] or transport of an electron through Luttinger liquid [29]. The advantage of the wave packets, is that it offers a very simple interpretation of the processes as well as a convenient framework for numerical time-dependent simulations.

From a practical point of view and to obtain relevant predictions, is desirable to introduce

source terms instead of single particles. During the last decades, the numerical approximations involving source terms has been drastically improved (see e.g. [30] and references therein). Recent numerical approximations of source terms ensure accurate simulations and exhibit essential properties, as robustness and stability [31]. In the present thesis we simplify the method for time independent potentials developed in [31], inverting the evolution matrices analytically by means of the Usmani Formula [32], which reduces drastically the computer effort. Additionally, we extent that result to the case of kicked potentials [33]. This approach, let us to study the transport properties of the quantum system in a more physical fashion. Here we fall into Floquet theory, which introduces a variety of tools to tackle the quantum dynamics of explicitly time periodic systems [34].

Here by means of the consideration of a simplified problem, we find that the mechanism responsible of the spin separation in the classical system, carries over to the quantized version. Taking into account the spatio-temporal symmetries of the system, and their breaking, the directed currents can be studied. The general problem is considered using the source term, in order to do the numerical simulation the most similar to a real experiment. In this case, the transmission and reflection coefficients can be calculated recording series of the amplitude probability at a fixed point to the right and the left of the numerical region respectively. From this data, we present conclusive evidence that also in the quantum system directed transport of spin and particles can be generated. Finally we show that far of the adiabatic limit, some specific set of parameters produces pure spin currents. We end this introduction with a brief introduction to the remaining chapters.

In chapter 2, we construct our model and justify its peculiarities. We discuss details of the dipole-field coupling that have not been considered previously in the context of chaotic scattering. Section 2.2 is dedicated to irregular scattering as the basic dynamical category of the system. Various diagnostics are presented such as deflection functions, unstable periodic orbits, and time-delay statistics. Our central subject, directed transport, is approached in section 2.3. We define relevant transport quantities in terms of reflection and transmission coefficients. Numerical evidence is provided for mass as well as for angular-momentum directed transport, and we point out the manifolds in parameter space where pure currents of either kind occur.

In chapter 3, we describe a numerical integration method for the time dependent Schrödinger equation and the implementation of the absorbing boundary conditions (ABC) and source terms into this integration scheme. In section 3.1, we simplify the numerical scheme inverting analytically the evolution matrices by means of the Usmani's formula for Jacobian matrices. Examples of propagating wave packets in the presence of potential barrier and well are presented. In section 3.2, we introduce the absorbing boundary conditions in to the integration scheme to compare the results with the perviously considered cases. We end this chapter, comparing our numerical results with the exact solution for the Schrödinger equation with source term in section 3.3.

In chapter 4, we describe the quantum stroboscopic evolution of an initial spin state in the presence of a kicked magnetic field. In section 4.2, we consider the case of a kicked magnetic field with a single component, and we calculate the transmission and reflection probabilities as a function of the period of the kicks τ. In section 4.2.2 we show that the multiphoton

absorption/emission process, inherent to every time periodic system, allows us to calculate the transmission probabilities and hence the currents in terms of the Floquet channels. In section 4.3 we present the plots of the evolution operator in momentum representation, and we solve the general problem with two perpendicular magnetic fields. We end this section demonstrating that the breaking of spatio-temporal symmetries gives rise to particle and spin currents, and that for certain set of parameters is even possible to generate pure spin current.

Finally in section 5, we present the conclusions and perspectives of the present thesis.

2 Classical Angular Momentum Pump

In this chapter, we study chaotic scattering and the possibility to generate directed transport of mass as well as angular momentum in a specific model. A magnetic dipole moving into a periodically modulated magnetic field confined to a compact region in space. We first introduce the model, justify its peculiarities and discuss details of the dipole-field coupling that have not been considered previously in the context of chaotic scattering. Then we derive the equations of motion and construct a stroboscopic map using time–discrete dynamics. This map will be useful to consider the time scales involved and the symmetries in our model. We then continue with a short review of the common properties inherent to every chaotic scattering system to corroborate that our model is an irregular scatterer in large parts of its parameter space. Finally, we show that if in addition to the mixed dynamics all spatio-temporal symmetries are broken, directed transport of mass as well as angular momentum occurs. The sensitive parameter dependence of the corresponding currents includes frequent sign reversals, giving rise in particular, to angular-momentum separation without mass transport as a classical analogue of spin-polarized currents.

2.1 Classical Model

2.1.1 Basic setup: Coupling internal to external freedoms

In constructing our model, we attempt to satisfy the following requirements, that the potential (*i*) couples the internal to the external degree of freedom, such that the dynamics of one freedom influences the other one (*ii*) vanishes identically outside a compact scattering region so that numerical simulations can be restricted to a spatial box of finite extension, and (*iii*) be periodically time dependent in the form of delta kicks in order to facilitate reducing the dynamics to a stroboscopic map.

Specifically, we choose the internal freedom as an intrinsic angular momentum (in the following of this chapter we shall also refer to it as spin, wherever its classical nature is obvious). In connection with a charge it gives rise to a magnetic dipole moment that couples to an external magnetic field and thus, if the field is not homogeneous, to the spatial motion

of the particle. However, we neglect the Lorentz force as concerns the transversal components of the spatial motion, which is justified as a good approximation if the longitudinal velocity is sufficiently small. In this respect, we treat the particle as neutral, in fact, neutrons would even provide a more natural physical realization of our model than electrons, reducing our model to a modified Stern-Gerlach setup.

Taking into account the previous criteria, the relevant dynamical variables are therefore the longitudinal coordinate x and its conjugate momentum p, as well as the spin vector $\mathbf{s} = (s_x, s_y, s_z)$. In terms of these variables, the Hamiltonian reads [9]

$$H(p, x, \mathbf{s}; t) = \frac{p^2}{2m_0} - \gamma\, \mathbf{B}(x, t) \cdot \mathbf{s}, \tag{2.1}$$

where m_0 is the particle's mass, $\mathbf{B}$ the magnetic field and γ the gyromagnetic ratio.

We choose the space and time dependence of the field as

$$\mathbf{B}(x, t) = (0, B_1(x), B_2(x)) \sum_{n=-\infty}^{\infty} \delta(n\tau - t - t_{\text{in}}), \tag{2.2}$$

with t_{in} a phase shift (c.f. 2.1.4 for details) and

$$B_1(x) = A_1 f(x + a/2), \quad B_2(x) = A_2 f(x - a/2), \tag{2.3}$$

and an envelope function

$$f(x) = \exp\left[\frac{-1}{(a/2)^2 - x^2}\right] \Theta\left[a/2 - |x|\right]. \tag{2.4}$$

This function vanishes outside the interval $[-a/2, a/2]$ yet is infinitely often differentiable.

2.1.2 Equations of motion

From the Hamilton equations,

$$\dot{p} = -\frac{\partial H}{\partial q}, \quad \dot{q} = \frac{\partial H}{\partial p} \tag{2.5}$$

we obtain the equations of motion (see Appendix A)

$$m_0 \ddot{\mathbf{x}} = \gamma \nabla(\mathbf{B} \cdot \mathbf{s}), \quad \dot{\mathbf{s}} = \gamma\, \mathbf{s} \times \mathbf{B}. \tag{2.6}$$

In all that follows, $m_0 = \gamma = \tau = 1$ is understood.

The field configuration defined in (2.3,2.4) implies that within the intervals $[-a, 0]$ and $[0, a]$, the field varies only in magnitude but not in direction. This allows for further simplifications. We identify the y-coordinate with the local field direction, $\mathbf{e}_y \equiv \mathbf{B}/B$, $B \equiv |\mathbf{B}|$,

choose spherical coordinates for the spin,

$$s_x = |\mathbf{s}| \sin\theta \sin\varphi, \quad s_y = |\mathbf{s}| \cos\theta, \quad s_z = |\mathbf{s}| \sin\theta \cos\varphi, \tag{2.7}$$

and denote $s \equiv |\mathbf{s}| = 1$. Then the y-component of the spin, $m \equiv s \cos\theta$, is the angular momentum canonically conjugate to the azimuth φ, while the polar angle θ becomes a constant of motion (see Appendix A), so that the spin dynamics reduces to a mere precession,

$$\ddot{x} = m\, \mathrm{d}B/\mathrm{d}x \qquad \dot{\varphi} = -B \tag{2.8}$$

with $m = \text{const}$.

For an inhomogeneous but unidirectional magnetic field, according to (2.8), the projection of the spin onto the field direction is a cyclic variable. This kind of dynamics therefore may give rise to chaotic spatial motion, but will not affect the spin. In order to induce "spin flips" (again abusing quantum terminology), we add a second interaction sector where the field is perpendicular to that in the first, as specified in (2.3) (see Fig. 2.1).

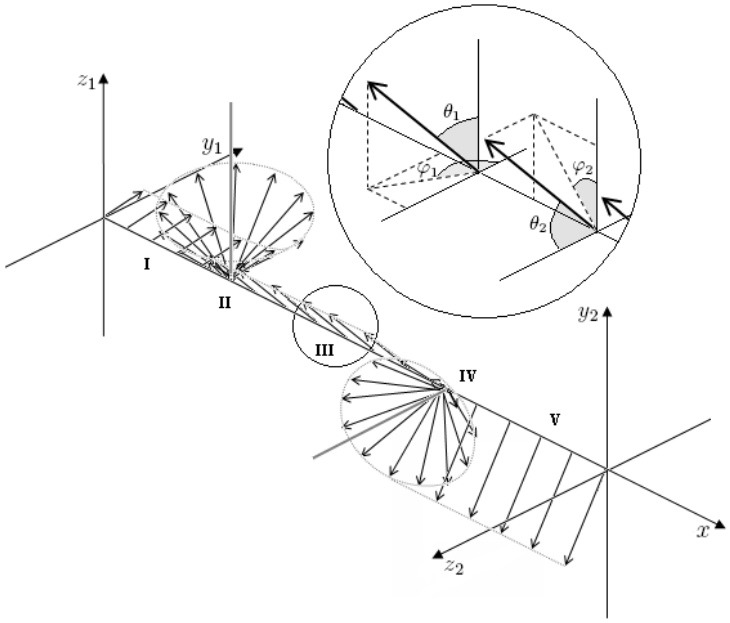

Figure 2.1: Schematic representation of the scattering process involving the spin vector $\mathbf{s}$ (bold arrows). In the incoming and outgoing asymptotic regions (phases I, V, resp.) $\mathbf{s}$ remains constant. Within the field sectors 1 and 2 (phases II and IV, resp.) it precesses around $\mathbf{B}$. Upon passing from sector 1 to 2 (phase III), the angles θ, ϕ defining the orientation of $\mathbf{s}$ undergo a passive transformation, as depicted in the enlargement (inset).

2.1.3 Symmetry considerations

The symmetries to be consider here may be further classified as: discrete spatial symmetries, discrete temporal symmetries and discrete spatio-temporal symmetries (involving changes in both space and time). With discrete, we mean a symmetry that describes non-continuous changes in the system, usually associated to reflections or interchanges. Specifically, we are interested in the invariance of the spatio-temporal symmetries under a simultaneous transformation of the form $x \to -x$ and $t \to -t$. Keeping in mind that the idea is to guarantee that the devised model breaks both of the inversion symmetries, let us consider first of all the spatial symmetry.

Upon passing from region 1 to 2 or back, the spherical coordinates (2.7) aligned with the field direction transform respectively as

$$\begin{aligned} \theta_2 &= \arccos(\sin\theta_1 \cos\varphi_1), \quad \theta_1 = \arccos(\sin\theta_2 \sin\varphi_2), \\ \varphi_2 &= \arctan(\cot\theta_1 \csc\varphi_1), \quad \varphi_1 = \arctan(\tan\theta_2 \cos\varphi_2). \end{aligned} \tag{2.9}$$

For identical widths and amplitudes of the two field sections, a spatial symmetry remains, namely rotation about the line through the origin and diagonal between the two field directions, see Fig. 2.2. In Cartesian coordinates, it corresponds to the transformation

$$x' = -x, \quad y' = z, \quad z' = y. \tag{2.10}$$

This symmetry would impede directed transport. In order to break it, we choose the two amplitudes distinct, $A_1 \neq A_2$, which gives the difference $A_2 - A_1$ the meaning of a symmetry-breaking parameter.

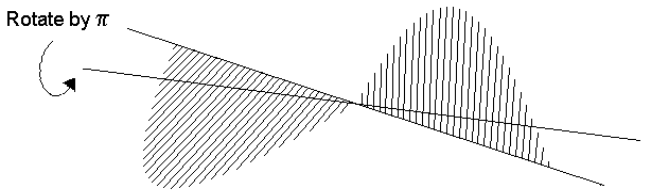

Figure 2.2: Configuration of the magnetic field, (2.3,2.4). In each of the two sectors 1 and 2, the field is isotropic, with an angle of $\pi/2$ between the two sectors. For equal amplitudes and identical envelopes, the field is symmetric with respect to rotation by π about the bold line, corresponding to the transformation (2.10). Rendering the widths and/or the amplitudes of the two field sectors different breaks this symmetry.

With respect to the symmetry of time, usually it can be understood by a simple analogy: if time were perfectly symmetric then it would be possible to watch a movie taken of real events and everything that happens in the movie would seem realistic whether it was played forwards or backwards. This is not the case in our particular problem, because despite the

movie played backward seems also realistic the system lacks of this symmetry. It could be clarified considering that there are some other variables which are negated by time reversal, i.e, if $t \to -t$, then the velocity, the linear momentum and the angular momentum are negated ($\vec{v} \to -\vec{v}$, $\vec{p} \to -\vec{p}$ and $\vec{l} \to -\vec{l}$). Back in to Eq. (2.6), we could easily note that the time reversal (together with the other negated variables) introduces an asymmetry through the spin dynamics, meaning that our system is not invariant under time reversal transformations.

2.1.4 Discrete-time dynamics

The impulsive driving allows us to integrate the equations of motion from one kick to the next. Placing time sections immediately before each kick, i.e., $t_n = n\tau - 0^+$, we arrive at the following stroboscopic maps for the two respective field regions

$$\begin{aligned} p_{n+1} &= p_n - 2x_{i,n}B_i(x_{i,n})\cos\theta_{i,n}/[(a/2)^2 - x_{i,n}^2]^2, \\ \varphi_{i,n+1} &= \varphi_{i,n} - B_i(x_{i,n})\,, \\ x_{i,n+1} &= x_{i,n} + p_{n+1}\,, \end{aligned} \tag{2.11}$$

where $i = 1, 2$, $B_i(x)$ refers to (2.3), $\varphi_{i,n}$ refers to the frames related by (2.9), and $x_{i,n} = x_n - (-)^i a/2$. One readily checks that these maps are canonical, that is, the determinant of their stability matrix equals unity.

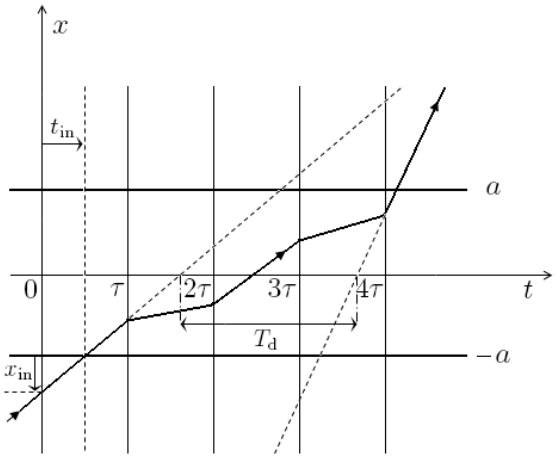

Figure 2.3: The phase $\phi_{\rm in}$ of a scattering trajectory (bold zigzag curve) relative to the periodic kicks of the driving (vertical lines) is defined with respect to the moment when it enters the scattering region at $x = \pm a$. It can alternatively be scaled as a time shift $t_{\rm in}$ or a spatial offset $x_{\rm in}$. By contrast, the definition of the delay time $t_{\rm d}$ refers to the extrapolation of the incoming and outgoing asymptotes (dotted lines) forward and backward, resp., till they intersect the line $x = 0$. See text for details.

In this periodically driven scattering system, the phase shift of an incoming trajectory

relative to the driving field appears as an additional scattering parameter [7, 8, 16]. It can be defined in various manners; for our particular case of an impulsive driving and a compact spatial support of the field we choose the time lag of the trajectory when it enters the field region at $x = \pm a$ with respect to the most recent kick at $t = n\tau$, cf. Fig. 2.3. By definition, its range is $0 \leq t_{\rm in} < \tau$. Equivalently, it can be rescaled as a spatial shift $x_{\rm in} = p_{\rm in} t_{\rm in}$, $0 \leq x_{\rm in} < p_{\rm in}\tau$, or a phase angle $\phi_{\rm in} = 2\pi t_{\rm in}/\tau$, $0 \leq \phi_{\rm in} < 2\pi$.

2.1.5 Time scales

The dynamics generated by (2.6) is characterized by three time scales: (*i*) the temporal separation of the kicks, which defines our unit of time, (*ii*) the period of spin precession, given by the inverse field strength B^{-1}, and (*iii*) the typical time to pass the scattering region, of the order of $a/p_{\rm in}$. As it is our objective to study the participation of the internal freedom in chaotic scattering, we shall work in a regime where all the three time scales are comparable. This prevents, in particular, using adiabatic approximations based on a slow motion of the external coordinate as compared to spin precession.

2.2 Chaotic scattering

In general terms *scattering* means a random distribution of certain items. In physics it has a different and quite definite meaning. We can define scattering as the problem of obtaining the relationship between an "input" variable (or variables) characterizing an initial condition for some dynamical system and an "output" variable (or variables) characterizing a suitable well defined final state of the system.

The simplest example of scattering deals with the motion of a point particle in a potential $V(x)$, where $V(x)$ is zero or else very small outside of some scattering region of finite extent. Lets define an input variable b (the impact parameter) and an output parameter ϕ (the scattering angle). The idea is to find a functional relationship between ϕ and b (the deflection function) in order to extract some information about the scatterer. The interesting point, is that this relationship is qualitatively different for the two cases where the dynamics in the scattering region is chaotic or non chaotic. If the scattering is non chaotic, the relation between ϕ and b is a simple smooth curve, if it is chaotic, typically we will find that the output variable ϕ varies too rapidly with the input variable b to be resolved.

Following the literature, we here consider chaotic scattering as defined by the following properties [35, 36, 37]: (*i*) rapidly fluctuating deflection functions with self-similar structure, at least in a statistical sense, and singularities accumulating towards the orbits of the chaotic repeller, (*ii*) the existence of a chaotic repeller consisting of a discrete set of unstable periodic orbits in the scattering region, and (*iii*) an exponential distribution of delay times inside the scattering region for a fully hyperbolic dynamics and an algebraic distribution for non-hyperbolic dynamics [38, 39]. In the subsequent paragraphs we present numerical evidence that the system devised above complies with all these criteria.

2.2.1 Deflection functions

In plotting the deflection functions we concentrate on two parameters as incoming variables: the phase ϕ_{in} as an important control parameter in experimental applications and the polar angle θ_{in} as we are interested in the directed transport of angular momentum and ought to make sure that this variable participates in the chaotic scattering.

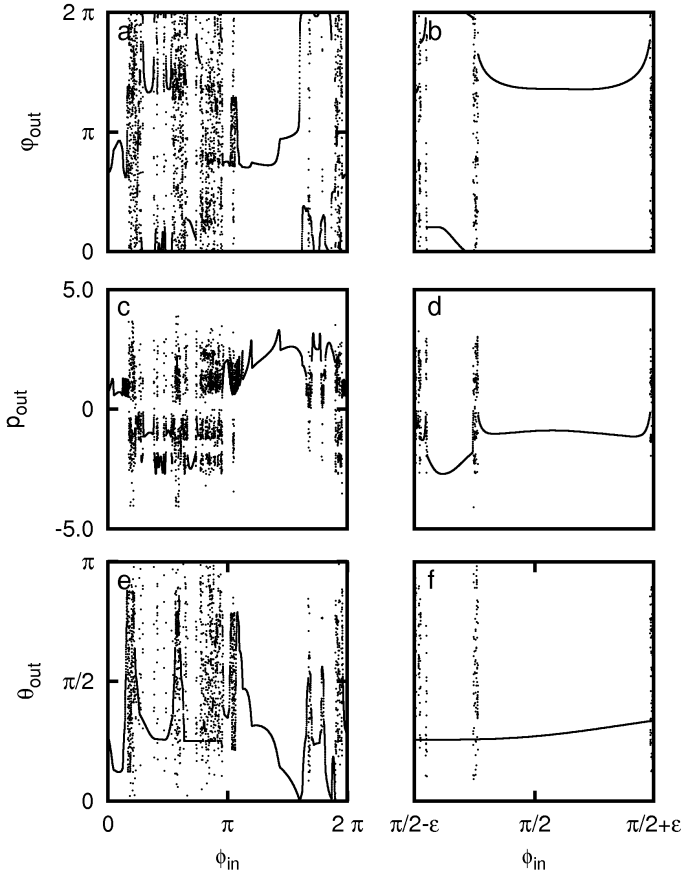

Figure 2.4: Deflection functions for the outgoing azimuth φ_{out} (a,b), outgoing linear momentum p_{out} (c,d), and outgoing polar angle θ_{out} (e,f) vs. initial phase ϕ_{in}. Figures (b,d,f) corresponds to a magnification of figures (a,c,e) respectively. The other initial conditions and parameters are $\varepsilon = 0.01$, $p_{\text{in}} = 1$, $\theta_{\text{in}} = \pi/4$ and $\varphi_{\text{in}} = 0$, $A_1 = 2$, $A_2 = 1$, $a = 4$.

In Figs. 2.4-2.5 (panels a,c,e) we plot the deflection function for the outgoing azimuth φ_{out}, outgoing linear momentum p_{out}, and outgoing polar angle θ_{out} as a function of the initial phase ϕ_{in} and the initial polar angle θ_{in} respectively. All these functions displays wild fluctuations which are conspicuous sing of chaotic behavior. Moreover, in Figs. 2.4-2.5 (panels b,d,f) we plot a magnification of a small section of each corresponding deflection function in the left hand side, it shows, that the typical oscillations of the deflection function occurs in all the scales of the incoming parameter variations. While these figures show the typical behavior

of a chaotic scatterer for large parts of the parameter space, we observe a clearly regular pattern in the right column of Fig. 2.5 (panels a,c,e) for $\theta_{\rm in} > \pi/2$ that calls for a special explanation. It reflects a strong asymmetry of the scattering process: Trajectories entering region 1 from the left, feel a strong repulsive force and bounce back immediately without ever passing into region 2, while trajectories coming in from the right undergo the typical irregular scattering with unbounded delay time. Such long trajectories tend to randomize the outgoing direction and thus lead to approximately balanced transmission and reflection probabilities. We shall see in section 2.3 that this asymmetry is largely responsible for the transport processes in the system.

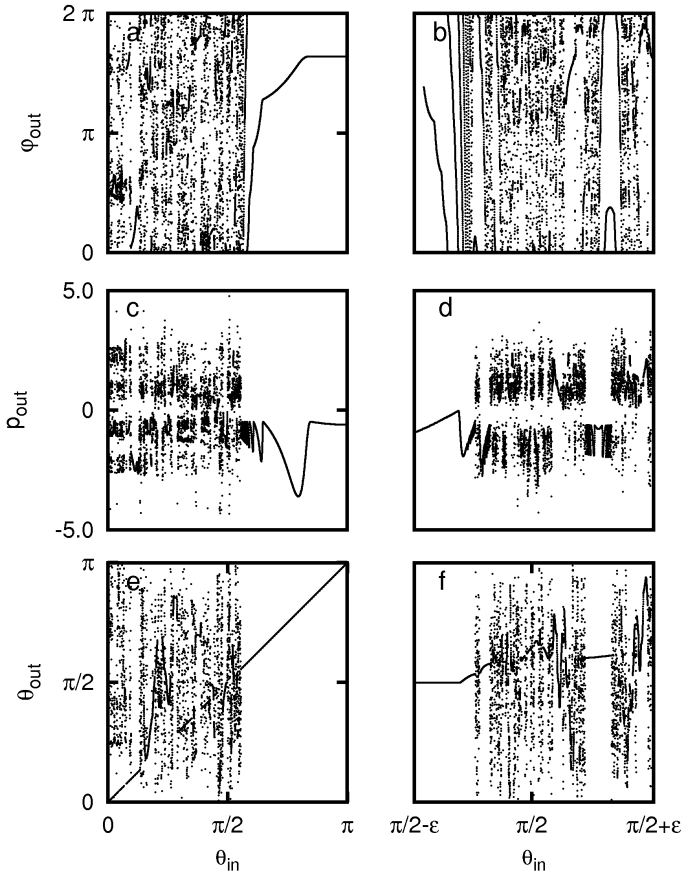

Figure 2.5: Deflection functions for the outgoing azimuth $\varphi_{\rm out}$ (a,b), outgoing linear momentum $p_{\rm out}$ (c,d), and outgoing polar angle $\theta_{\rm out}$ (e,f) vs. initial polar angle $\theta_{\rm in}$. Each figure in the right hand side corresponds to a zoom of the respective figure in the left hand side. The other initial conditions and parameters are $\varepsilon = 0.01$, $p_{\rm in} = 0.5$, $\phi_{\rm in} = 0$ and $\varphi_{\rm in} = 0$, $A_1 = 2$, $A_2 = 1$, $a = 4$.

2.2.2 Stable and unstable periodic orbits

A periodic orbit corresponds to a special type of solution for a dynamical system, namely one which repeats itself in time. In the case of a discrete map, $x_{i+1} = f(x_i)$, a periodic orbit with period k, is the set of k distinct points with $f^k(x_0) = x_0$ (see Fig. 2.6 (panel a)), where f^k represents the composition of f with itself k times. The smallest positive value of k for which this equality holds is the period of the orbit.

The stability of a periodic orbit for an autonomous vector field can be calculated by considering the Poincaré map, which can be interpreted as a discrete dynamical system with a state space that is one dimension smaller than the original continuous dynamical system. Specifically, an $(n-1)$-dimensional surface of section Σ is chosen such that the flow is always transverse to Σ (see Fig. 2.6 (panel b)).

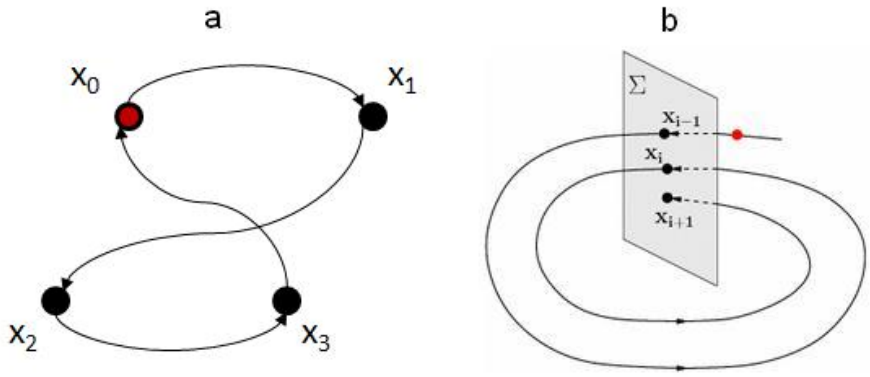

Figure 2.6: Periodic orbit for a map (Panel a). Poincaré map for a vector field (Panel b).

Let the successive intersections in a given direction of the solution $x(t)$ with Σ be denoted by x_i. The Poincaré map

$$x_{i+1} = g(x_i),$$

determines the $(i+1)$-th intersection of the trajectory with Σ from the i-th intersection. A periodic orbit of an autonomous vector field corresponds to a fixed point x_f of this Poincaré map. The linearization of the Poincaré map about x_f is

$$\xi_{i+1} = \mathrm{D}g(x_f)\xi_i.$$

If all eigenvalues of Dg have modulus less than unity, then x_f (and thus the corresponding periodic orbit) is asymptotically stable. If any eigenvalues of Dg have modulus greater than unity, then x_f (and thus the corresponding periodic orbit) is unstable.

With the aim of illustration, in Fig. 2.7 we depict an unstable periodic orbit (a) that belongs to the chaotic repeller and a stable one (b) that is inaccessible from outside the scattering region . They are marked by symbols $\times$ and $+$, resp., in Fig. 2.8a. While for the former, the spin exhibits a significant motion that cannot even be reduced to mere precession,

for the latter it remains at rest. In orbital phase space, this orbit forms a double loop, but the corresponding self-crossing is lifted upon taking the spin motion into account.

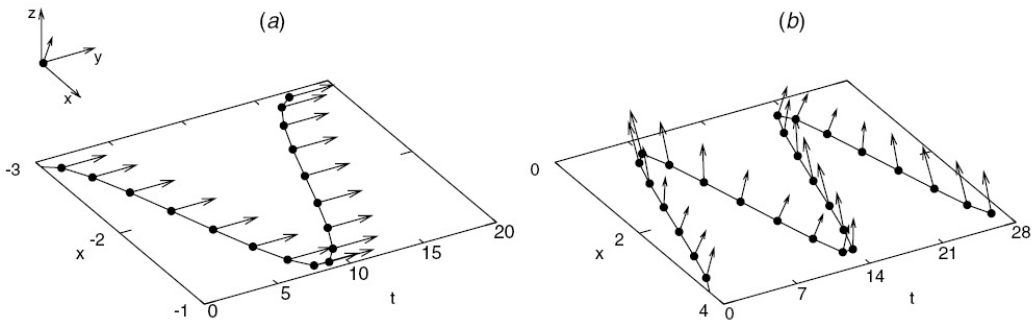

Figure 2.7: Examples of an unstable (a) and a stable (b) periodic orbit, located respectively in the chaotic region (marked by $\times$) and in the left stable island in Fig. 2.8 (marked by $+$). The spatial motion is shown as position x vs. continuous time t, the spin orientation at each t_n in an independent 3-dim. coordinate system moving with the spatial trajectory (inset). While the stable orbit leaves the spin at rest parallel to the field, the unstable one involves a significant spin motion.

On the other hand, from (2.11) it is evident that the polar angle θ plays a decisive rôle for the dynamics as its sign determines the local stability of a trajectory. Specifically, upon passing from one field region to the other, the dynamics turns elliptic or hyperbolic according to whether $\cos\theta_{\rm in}$ is positive or negative, respectively (see Fig. 2.8).

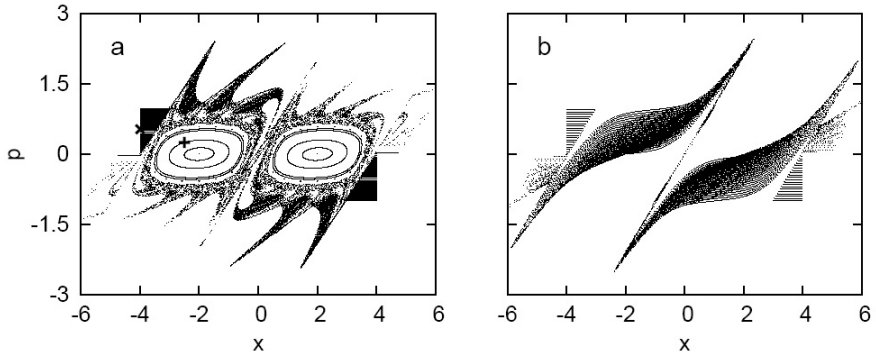

Figure 2.8: Poincaré sections in the (x,p)-plane for positive (panel a) vs. negative (b) incoming polar angle $\theta_{\rm in}=-\pi/4$ (b). The other initial conditions and parameters are $\phi_{\rm in}=0$, $\varphi_{\rm in}=0$, $A_1=A_2=1$ and $a=4$. The large regular areas in panel a correspond to stable islands not accessible from outside the scattering region.

2.2.3 Delay-time statistics

We define the delay time $T_{\rm d}$ for a given scattering trajectory, as the time difference between the incoming and outgoing asymptotes extrapolated forward and backward respectively till the origin, cf. Fig. 2.3, or in other words, as the time spent by the particle within the interaction region when the potential is turned on $t_{\rm on}$, minus the time spent by the particle within the interaction region when the potential is turned off $t_{\rm off}$, $T_{\rm d} = t_{\rm on} - t_{\rm off}$.

The delay time is strongly related to the complexity of the deflection function as we explain in the following. In general, every scattering system have infinitely many orbits trapped in the interaction region, some of them are periodic and some are aperiodic. In practice, the stable periodic orbits can be reached choosing initial conditions inside the scattering region, then an incoming particle form the asymptotic region which enters into the scattering region follows for some arbitrary time a chaotic orbit, or a regular one but non periodic, till it scatters out. The closer it gets to a trapped periodic orbit the longer it stays in the interaction region. In that sense, a deflection function region with a wildly fluctuating behavior corresponds to a longer time delay, which is related to a unstable periodic orbit for the longer time.

There is another fundamental aspect to be noted, that is the dependence of the time delay statistics $P(T)$ with the dynamics. Imagine that we pick many b values at random in some interval. We then examine the resulting orbit from each value and determine the time T that this orbit spends in the scattering region. The fraction of orbits with time delays between T and $T + dT$ is $P(T)dT$. For hyperbolic dynamics in the scattering region, one finds that for large T the time delay statistics decays exponentially,

$$P(T) \sim \exp(-T/\tau)$$

where τ is a characteristic time of the scatterer. While for chaotic dynamics with bounding KAM surfaces in the scattering region, there is a qualitatively different behavior in which $P(T)$ decays algebraically

$$P(T) \sim T^{-\alpha}.$$

In Fig. 2.9 we show the delay time statistics as a function of the initial phase $\phi_{\rm in}$ and the incoming polar angle $\theta_{\rm in}$, for the same parameters used in Figs. 2.4-2.5. We easily note the algebraic decay of $P(T)$ due to the non-hyperbolic dynamics of the system for such set of parameters.

2.3 Directed transport

Previous work on nonlinear transport mechanisms in ratchets and pumps has revealed two fundamental necessary (though not sufficient) conditions for directed currents to occur [12, 13, 14, 15, 16]: An inhomogeneous phase space (e.g., a mixed dynamics where regular coexists with chaotic motion) and the absence of any spatio-temporal symmetry that would rise to pairs of otherwise identical trajectories carrying the same current in opposite directions.

We have shown in the preceding sections that our model fulfills the two necessary con-

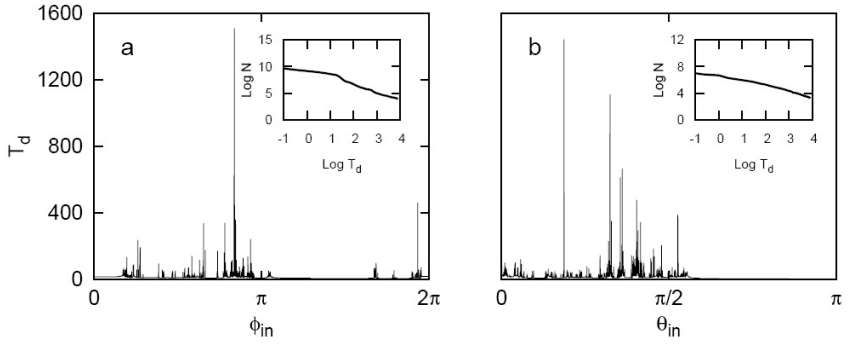

Figure 2.9: Delay-time statistics as a function of initial phase $\phi_{\rm in}$ (a) and incoming polar angle $\theta_{\rm in}$ (b). The other initial conditions and parameters are $p_{\rm in} = 1.0$, $\theta_{\rm in} = \pi/4$ (a), $p_{\rm in} = 0.5$, $\phi_{\rm in} = 0$ (b), and $\varphi_{\rm in} = 0$, $A_1 = 2$, $A_2 = 1$, $a = 4$. Insets: the respective accumulated probability distributions for $T_{\rm d}$.

ditions for directed transport mentioned above, inhomogeneous phase space and absence of binary spatio-temporal symmetries, and therefore expect to find directed currents at least in parts of its parameter space.

2.3.1 Asymmetric scattering and directed currents

In the context of a scattering system, we define the current as the frequency of particles leaving the scattering region to the right minus the frequency of particles leaving to the left. Denoting $T_{\alpha\beta}$ the fraction of particles transmitted from "channel" α to β and $R_{\alpha\alpha}$ the fraction of particles reflected from α back into α, with $\alpha, \beta =$ "l" (left) or "r" (right), the current is given by (see e.g. Appendix B and [16])

$$I = (T_{\rm lr} + R_{\rm rr} - R_{\rm ll} - T_{\rm rl})\,. \tag{2.12}$$

In the context of quantum electronics, the spin current is given simply as the difference between the currents in the two spin states "up" vs. "down", $I_{\rm s} = I_\uparrow - I_\downarrow$, with the partial currents defined in turn as in (2.12). As an immediate generalization to a larger total spin we would write the spin current as a weighted sum of partial currents, with the weights given by the projection of the spin onto some appropriate direction of reference. This suggests to define the spin current in a classical context (see Appendix C), where the angular momentum is continuous, as a weighted integral over partial currents parameterized by spherical coordinates,

$$I_{\rm s} = \frac{1}{4\pi}\int_0^\pi {\rm d}\theta \sin\theta \int_{-\pi}^{\pi} {\rm d}\varphi \cos\theta\, j(\theta,\varphi), \tag{2.13}$$

with the current density

$$j(\theta,\varphi) = (j_{\rm lr}(\theta,\varphi) + j_{\rm rr}(\theta,\varphi) - j_{\rm ll}(\theta,\varphi) - j_{\rm rl}(\theta,\varphi))\,, \tag{2.14}$$

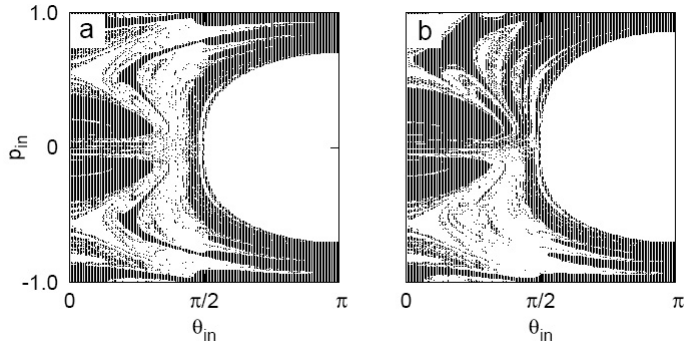

Figure 2.10: Qualitative outcome of scattering, i.e., transmission (black) vs. reflection (white) as a function of two initial conditions, $\theta_{\rm in}$ and $p_{\rm in}$, for a configuration with (a) and without (b) the spatial symmetry (2.10). The other initial conditions and parameters are $A_1 = 1$ (a), $A_1 = 2$ (b), and $A_2 = 1$, $a = 4$, $\phi_{\rm in} = 0$, $\varphi_{\rm in} = 0$.

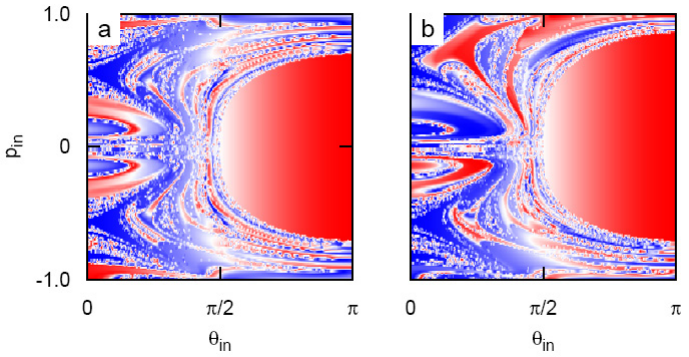

Figure 2.11: Effective outgoing spin $\cos\theta_{\rm out}$ (red ≡ negative, white ≡ zero, blue ≡ positive) as a function of incoming polar angle $\theta_{\rm in}$ and linear momentum $p_{\rm in}$, for a configuration with (a) and without (b) the spatial symmetry (2.10). The other initial conditions and parameters are $A_1 = 1$ (a), $A_1 = 2$ (b), and $A_2 = 1$, $a = 4$, $\phi_{\rm in} = 0$, $\varphi_{\rm in} = 0$.

using obvious shorthands for the partial currents between the respective leads. The angles should refer to some suitable laboratory frame, here chosen as the system corresponding to field region 1, cf. (2.3).

We here assume an initially unpolarized ensemble, corresponding to a homogeneous angular-momentum distribution over the unit sphere. In some cases it is preferable to fix part or all of the initial conditions and to analyze the transport properties as a function of these variables. In Figs. 2.10 and 2.11, we show respectively the outcome of the scattering process, i.e., transmission vs. reflection, and the polarization of the outgoing particles as functions of the initial polar angle and linear momentum. Also in these quantities we observe fractal self-similar structures as in the deflection functions, and a correspondingly sensitive parameter dependence. The presence (panels a) or absence (panels b) of the symmetry (2.10) is clearly reflected in the transport features. The large almost void regions that appear in

all graphs for $\theta_{\rm in} > \pi/2$ correspond to trajectories that bounce back immediately after entry, while manifestly asymmetric structures are found only for $\theta_{\rm in} < \pi/2$. This confirms the mechanism described in section 2.2.1, that chaotic randomization of the outgoing direction occurs only for particles spinning in one sense but not for the other.

The occurrence of directed transport in this system manifestly violates linear-response theory. In terms of static quantities, we are dealing with a non-zero mean (direct) current in the absence of any external mean gradient. Even if we allow for time-dependent input and output, the fact that the system is driven periodically through a single parameter would entail an exact cancelation of transport in a linear-response treatment. The same conclusion results from a Taylor expansion of the current in terms of the driving frequency ω,

$$I(\omega) = I_0 + I_1\omega + O(\omega^2). \tag{2.15}$$

If only the I_1-term were present (linear response), time reversal of the driving $\omega \to -\omega$ would lead to an exact reversal of the current ("turning the crank backwards pumps in the opposite direction"). In our case, the driving is inherently symmetric in time so that the presence of a directed current is incompatible with linear response [16]. We emphasize that the functional dependence of the current output on the driving amplitude is irrelevant for this conclusion.

The dependence of the polarization on width and amplitude of the field Fig. 2.12a, demonstrates how the spin output could be controlled varying these two parameters that are easily accessible in experiments. The rôle of the symmetry is more directly revealed in Fig. 2.12b where the diagonal $A_1 = A_2$ coincides with a zero of the polarization. There are, however, other conspicuous zones of vanishing polarization apparently unrelated to this symmetry.

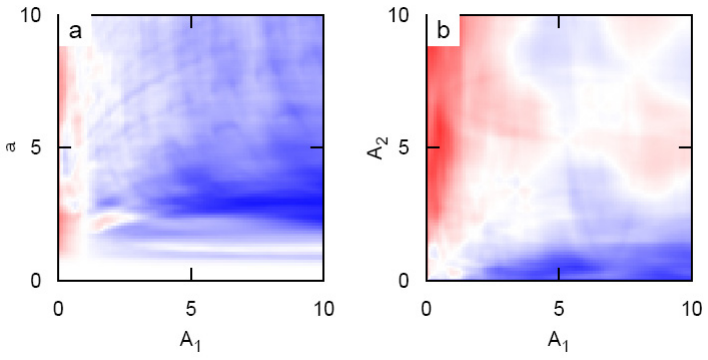

Figure 2.12: Effective outgoing spin $\cos\theta_{\rm out}$ (red ≡ negative, white ≡ zero, blue ≡ positive) as a function of width a and amplitude A_1 of the left field sector (a) and of the amplitudes A_1 and A_2 (b), averaged over $\theta_{\rm in}$ and $p_{\rm in}$. The other initial conditions and parameters are $A_2 = 1$ (a), $a = 4$ (b), $\phi_{\rm in} = 0$ and $\varphi_{\rm in} = 0$.

2.3.2 Angular-momentum transport

The data presented in Figs. 2.11 and 2.12 strongly indicate the existence of polarized currents at least in certain regions of the parameter space. We sketch in Fig. 2.13 how a separation of spins could come about in principle in the absence of a net mass current. In order to corroborate its robustness and experimental feasibility, we show in Figs. 2.14, 2.15 global averages both of the particle and the spin current, cf. (2.12,2.13). We find zeros of the spin current I_s at appreciable values of the particle current I, corresponding to unpolarized charge transport, as well as zeros of I at high values of I_s. These latter cases amount to a separation of different orientations of angular momentum without net particle transport, that is, the classical analogue of spin filtering or rectification.

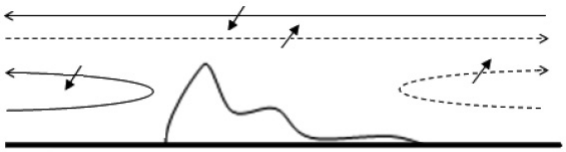

Figure 2.13: A finite spin current in absence of net mass (charge) transport can arise if particle currents cancel due to parity invariance between transmission and reflection from either side, while the corresponding coefficients for spin scattering lack this symmetry. In this schematic figure, all particles with spin down (full lines) leave to the left, irrespective of the incoming direction, while those with spin up (dotted) all leave towards the right. At the same time, if all currents are assumed to have the same magnitude, mass transport vanishes identically, resulting in pure spin separation.

Moreover, in Fig. 2.14 we observe a strong dependence of this phenomenon on the breaking of parity, in terms of the ratio A_1/A_2. As discussed in 2.1.3 above, it must vanish for $A_1 = A_2$. At the same time, we expect it to diminish in the opposite extreme of $A_1 \ll A_2$ or v.v., as in this limit the effect of the two regions with different field orientation breaking the symmetry (2.10) is lost. Therefore there should exist an optimum for angular momentum separation at intermediate values of A_1/A_2.

2.4 Summary

In this chapter we demonstrate the possibility of pumping angular momentum in a fast and strong driven chaotic scattering system. The transport of mass and angular momentum we observe, is attributable to the simultaneous effect of the nonlinear dynamics and the breaking of spatio-temporal symmetries and do not require a two-parameter driving as in adiabatic pumping. Through a simple model we have showed how an internal degree of freedom not only participates in chaotic scattering, but even gives rise to new phenomena, namely, the fact that spin separation clearly corresponds to a reduction of entropy.

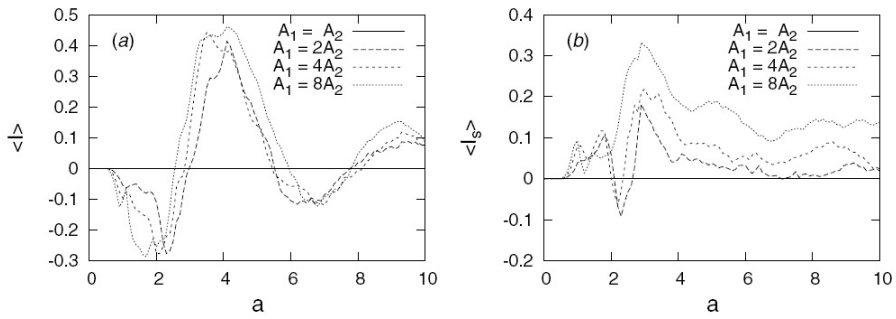

Figure 2.14: Particle current I (panel a) and spin current $I_{\rm s}$ (b), averaged over $\theta_{\rm in}$ and $p_{\rm in}$ vs. the width of the well a for various values of the ratio A_1/A_2. Parameters are $A_2 = 1$ and $\varphi_{\rm in} = 0$.

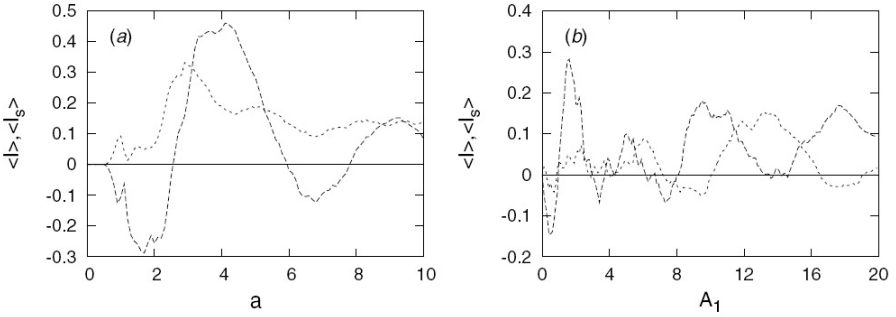

Figure 2.15: Comparison of particle current I (broken curve) to spin current $I_{\rm s}$ (dotted), averaged over $\theta_{\rm in}$ and $p_{\rm in}$, as functions of the width a of the scattering region (panel a) and the mean magnetic field strength (panel b). Parameters are $\varphi_{\rm in} = 0$ and $A_1 = 8$, $A_2 = 1$ (panel a) and $a = 4$, $A_1/A_2 = 1.5$ (b).

The classical study presented in this chapter is a preparatory survey aiming towards chaotic spin pumping. On grounds of semiclassical arguments, we would expect the mechanisms we elucidate to carry over at least to a "mildly" quantum regime. The electron spin, however, corresponds to the deep quantum limit where among other consequences, the assumption of a slow spin precession, comparable to the other time scales in the system, no longer applies. In order to address this question, we depict in Fig. 2.15b mass and spin currents as a function of the magnetic field strength, equivalent to the precession frequency, at constant asymmetry. We see that directed transport does not diminish significantly and we even find instances of pure spin current in a regime where both time scales differ by more than an order of magnitude, giving us some confidence that chaotic pumping of angular momentum could extend down to $s = \hbar/2$.

3 Wave–Packet Evolution

In this chapter, we describe a numerical integration method for the time–dependent Schrödinger equation and the implementation of the absorbing boundary conditions (ABC) and source terms into this integration scheme. All the calculation are based on the procedure and results of Paul et al. [31], nonetheless, we simplify the numerical scheme by inverting analytically the matrices of the evolution operator in position representation by means of the Usmani's formula for Jacobian matrices [32]. The analytical inversion of the matrices reduces drastically the computational effort, which is desirable for the case of time–dependent potentials in which the matrices vary in every time step. Here, we consider the case of time–independent potentials, but we sketch the theory as a preparatory survey for the next section in which we apply it to the particular case of kicked potentials. We begin by describing the method and presenting the formula for the inverse of non–symmetrical tridiagonal Jacobian matrix. We show how to introduce the inverse matrix formulas into the numerical scheme. We then continue relating it to the absorbing boundary conditions to finally apply it for the case of the source term. We end this chapter comparing our numerical results with the exact solution for the Schrödinger equation with source term.

3.1 The Method

Let us consider the Schrödinger equation in atomic units, i.e. $m = \hbar = 1$,

$$i\frac{\partial}{\partial t}\psi(x,t) = H(x,t)\psi(x,t), \tag{3.1}$$

with the Hamiltonian given by

$$H(x,t) = -\frac{1}{2}\frac{\partial^2}{\partial x^2} + V(x,t). \tag{3.2}$$

What we aim for, is to compute the time evolution of the wave function $\psi(x,t)$ for $t > t_0$ given an initial state $\psi(x,t_0)$. Then, we divide the time interval into n equal parts of size

$\Delta t = (t - t_0)/n$, and use an implicit Crank–Nicholson integrator scheme [40] to propagate the wave function from one time step to the next one.

The formal solution to (3.1) could be expressed in terms of the time evolution operator $U = e^{-iHt}$ as,

$$\psi(x,t) = e^{-iHt}\psi(x,0). \tag{3.3}$$

The effective time–evolution operator U for one discrete time step Δt can be expressed using Cayley's form for the finite-difference representation of e^{-iHt}, which is a combination of a fully implicit and a fully explicit method [41],

$$U(t+\Delta t,t) = \left(1 - \frac{i\Delta t}{2}H(x,t)\right) / \left(1 + \frac{i\Delta t}{2}H(x,t)\right), \tag{3.4}$$

such representation of U is second-order accurate in space and time and also unitary. The integration scheme for the wave function then reads

$$\left(1 + \frac{i\Delta t}{2}H(x,t)\right)\psi(x,t+\Delta t) = \left(1 - \frac{i\Delta t}{2}H(x,t)\right)\psi(x,t)\,. \tag{3.5}$$

The wave function can be expanded on a discrete lattice as

$$\psi(x,t_n) = \sum_{j=1}^{N} \psi_j^n \chi_j\,, \tag{3.6}$$

where $\psi_j^n = \psi(x_j,t_n)$ is the value of the wave function at the position x_j of the jth lattice site at time $t_n = t_0 + n\Delta t$, with a grid basis

$$\chi_j = \begin{cases} 1, & x_j - \frac{1}{2}\Delta x \le x \le x_j + \frac{1}{2}\Delta x; \\ 0, & \text{otherwise.} \end{cases} \tag{3.7}$$

Here $\Delta x = (x_{max} - x_{min})/N$, and (x_{max}, x_{min}) are the boundaries of the finite grid.

Using the finite-difference representation for the kinetic part of the hamiltonian, we have

$$\left(1 \pm \frac{i\Delta t}{2}H\right)\psi(x_j,t_n) \simeq \psi_j^n \pm \frac{i\Delta t}{2}\left(-\frac{\psi_{j+1}^n - 2\psi_j^n + \psi_{j-1}^n}{2\Delta x^2} + V_j^n\psi_j^n\right) \tag{3.8}$$

with $V_j^n = V(x_j,t_n)$. By introducing $\vec{\psi}^n = (\psi_1^n, ..., \psi_j^n, ..., \psi_N^n)$, the lattice representation of Eq. (3.5) finally reads

$$\mathbf{D}_2\vec{\psi}^{n+1} = \mathbf{D}_1\vec{\psi}^n \Leftrightarrow \vec{\psi}^{n+1} = \mathbf{D}_2^{-1}\mathbf{D}_1\vec{\psi}^n\,, \tag{3.9}$$

where we define

$$\mathbf{D}_1 = \left(1 - \frac{i\Delta t}{2}H\right) = (1 - \mathbf{S}), \quad \mathbf{D}_2 = \left(1 + \frac{i\Delta t}{2}H\right) = (1 + \mathbf{S}), \tag{3.10}$$

with $\mathbf{S} = \frac{i\Delta t}{2} H$. The matrix product can be rewritten as

$$\begin{aligned}
\mathbf{D}_2^{-1}\mathbf{D}_1 &= (1+\mathbf{S})^{-1}(1-\mathbf{S}) \\
&= (1+\mathbf{S})^{-1} - (1+\mathbf{S})^{-1}\mathbf{S} + (1+\mathbf{S})^{-1} - (1+\mathbf{S})^{-1} \\
&= 2(1+\mathbf{S})^{-1} - (1+\mathbf{S})^{-1}(1+\mathbf{S}) \\
&= 2(1+\mathbf{S})^{-1} - 1 \\
&= 2\mathbf{D}_2^{-1} - 1, \qquad (3.11)
\end{aligned}$$

it means, that the wave–packet evolution is achieved just by inverting the matrix $\mathbf{D}_2$.

In the general case of time–dependent potentials, the explicit $N \times N$ representation of $\mathbf{D}_1$ and $\mathbf{D}_2$ reads

$$\mathbf{D}_1 = \begin{pmatrix}
\gamma_1^n & \alpha & & & & \\
\alpha & \gamma_2^n & \alpha & & & \\
 & \alpha & \gamma_3^n & \alpha & & \\
 & & \ddots & \ddots & \ddots & \\
 & & & \alpha & \gamma_{N-1}^n & \alpha \\
 & & & & \alpha & \gamma_N^n
\end{pmatrix} \qquad (3.12)$$

$$\mathbf{D}_2 = \begin{pmatrix}
\xi_1^n & -\alpha & & & & \\
-\alpha & \xi_2^n & -\alpha & & & \\
 & -\alpha & \xi_3^n & -\alpha & & \\
 & & \ddots & \ddots & \ddots & \\
 & & & -\alpha & \xi_{N-1}^n & -\alpha \\
 & & & & -\alpha & \xi_N^n
\end{pmatrix} \qquad (3.13)$$

with

$$\alpha = \frac{i\Delta t}{4\Delta x^2}, \;\; \gamma_j^n = 1 - \beta_j^n \;\; \xi_j^n = 1 + \beta_j^n, \;\; \text{and} \;\; \beta_j^n = \frac{i\Delta t}{2}\left(\frac{1}{\Delta x^2} + V_j^n\right). \qquad (3.14)$$

For the case of time–independent potentials, the matrices $\mathbf{D}_1$ and $\mathbf{D}_2$ are constants and the parameters are given by

$$\alpha = \frac{i\Delta t}{4\Delta x^2}, \;\; \gamma_j = 1 - \beta_j \;\; \xi_j = 1 + \beta_j, \;\; \text{and} \;\; \beta_j = \frac{i\Delta t}{2}\left(\frac{1}{\Delta x^2} + V_j\right). \qquad (3.15)$$

In the next section we calculate the inverse of a complex tridiagonal matrix analytically in order to simplify this problem.

3.1.1 Inverse of a Tridiagonal Matrix

Let us consider the $N \times N$ non–singular tridiagonal matrix $\mathbf{D}$

$$\mathbf{D} = \begin{pmatrix} a_1 & b_1 & & & & \\ c_1 & a_2 & b_2 & & & \\ & c_2 & a_3 & b_3 & & \\ & & \ddots & \ddots & \ddots & \\ & & & c_{N-2} & a_{N-1} & b_{N-1} \\ & & & & c_{N-1} & a_N \end{pmatrix} . \tag{3.16}$$

In [32], Usmani gave an elegant and concise formula for the inverse of the tridiagonal matrix

$$(\mathbf{D})^{-1}_{ij} = \begin{cases} (-1)^{i+j} b_i \dots b_{j-1} \theta_{i-1} \phi_{j+1} / \theta_N, & i \le j\,; \\ (-1)^{i+j} c_j \dots c_{i-1} \theta_{j-1} \phi_{i+1} / \theta_N, & i > j\,, \end{cases} \tag{3.17}$$

where θ_i's verify the recurrence relation

$$\theta_i = a_i \theta_{i-1} - b_{i-1} c_{i-1} \theta_{i-2}, \qquad \text{for} \qquad i = 2, \dots, N, \tag{3.18}$$

with initial conditions $\theta_0 = 1$ and $\theta_1 = a_1$, and ϕ_i's verify the recurrence relation

$$\phi_i = a_i \phi_{i+1} - b_i c_i \phi_{i+2}, \qquad \text{for} \qquad i = N-1, \dots, 1, \tag{3.19}$$

with initial conditions $\phi_{N+1} = 1$, $\phi_N = a_N$ and with $\theta_N = \det \mathbf{D}$.

Applying the last procedure to the matrix $\mathbf{D}_2$, we obtain a simplified formula for the inverse,

$$(\mathbf{D}_2)^{-1}_{ij} = d_{ij} = (-1)^{i+j} (-\alpha)^{|j-i|} \theta_{i-1} \phi_{j+1} / \theta_N, \quad \text{if} \quad i \le j \tag{3.20}$$

due to the tridiagonal symmetric nature of $\mathbf{D}_2$, we get for the inverse ($d_{ji} = d_{ij}$). The recurrence relations are given by

$$\theta_i = \xi_i \theta_{i-1} - \alpha^2 \theta_{i-2}, \qquad \text{for} \qquad i = 2, \dots, N, \tag{3.21}$$

and

$$\phi_i = \xi_i \phi_{i+1} - \alpha^2 \phi_{i+2}, \qquad \text{for} \qquad i = N-1, \dots, 1, \tag{3.22}$$

with $\theta_0 = 1$, $\theta_1 = a_1$, $\phi_{N+1} = 1$ and $\phi_N = a_N$.

Finally, the elements of the matrix product $\mathbf{E} = \mathbf{D}_2^{-1} \mathbf{D}_1 = 2\mathbf{D}_2^{-1} - 1$, are given by

$$(\mathbf{E})_{ij} = 2\, d_{ij} - \delta_{ij} \quad \text{for} \quad i, j = 1, \dots, N\,, \tag{3.23}$$

where δ_{ij} is the Kronecker delta.

In order to test the method, in the next sections we consider two standard systems belonging to the class of time–independent potentials, the rectangular potential well and the

rectangular potential barrier. In both cases Dirichlet boundary conditions are assumed , i.e., the wave function is set to zero at the the boundaries of the grid. These boundary conditions may cause unwanted reflections. Therefore we have to perform the numerical calculations on a sufficiently large bounded interval, placing the impinging particle far away of the border and restricting the time interval such that the reflections do not affect the solution in the region of interest. The comparison between the numerical and analytical solutions is made through the transmission probabilities.

In all that follows, we treat the transmission and reflection events by following the time evolution of the wave packet as it move into and out the region of the potentials. It is well known that the initial wave packet can be chosen in a variety of ways, the choice being dictated largely by convenience. Here, we have elected to represent the initial state of the particle which impinges upon the potential by a Gaussian wave–packet centered about $x = x_0$,

$$\psi(x,0) = \sqrt[4]{\frac{1}{\pi}} \exp\left[ip_0(x-x_0) - \frac{(x-x_0)^2}{2}\right]. \tag{3.24}$$

3.1.2 Particle Scattered from a Finite Square Potential Well

As a first example to test the method and to see the effect of the Dirichlet boundary conditions, we consider a Gaussian wave–packet Eq. (4.34) initially centered at x_0, with average momentum p_0, which moves into the region of a short range defined as

$$V(x) = \begin{cases} -p_0^2/2, & -x_\mathrm{b} < x < x_\mathrm{b}; \\ 0, & \text{otherwise.} \end{cases} \tag{3.25}$$

This is an attractive square well whose depth equals the average energy $p_0^2/2$ of the Gaussian wave–packet [42].

For the numerical calculations we generate an one-dimensional list of complex numbers which represents the values of the initial wave function $\psi(x,0)$ on the points of the space grid (see Eq. 3.7), together with a one-dimensional list of real numbers which represents the values of the potential $V(x)$ on the points of the space grid Eq. (3.7). In this case the parameters are given by Eq. (3.15) with $V_j = V(x_j)$. In Fig 3.1 we show the Gaussian wave–packet scattering.

As was expected there exists a strong back reflection effect due to the Dirichlet boundary conditions, i.e. the wave packet behaves like inside a large infinite square well of length $L = 2x_{max}$. This kind of situation imposes limitations on the choice of the input parameters, e.g. x_0 and σ_0 in (4.34) must be chosen so that $\psi(-L/2,0)$ and $\psi(L/2,0)$ are essentially zero at the beginning $t = t_0$, and also in the output parameters, namely, when a wave packet spreads quickly any reflected portion of the wave will then interfere with the portion of the wave incident, giving rise to a non-physical interference pattern but a numerical one.

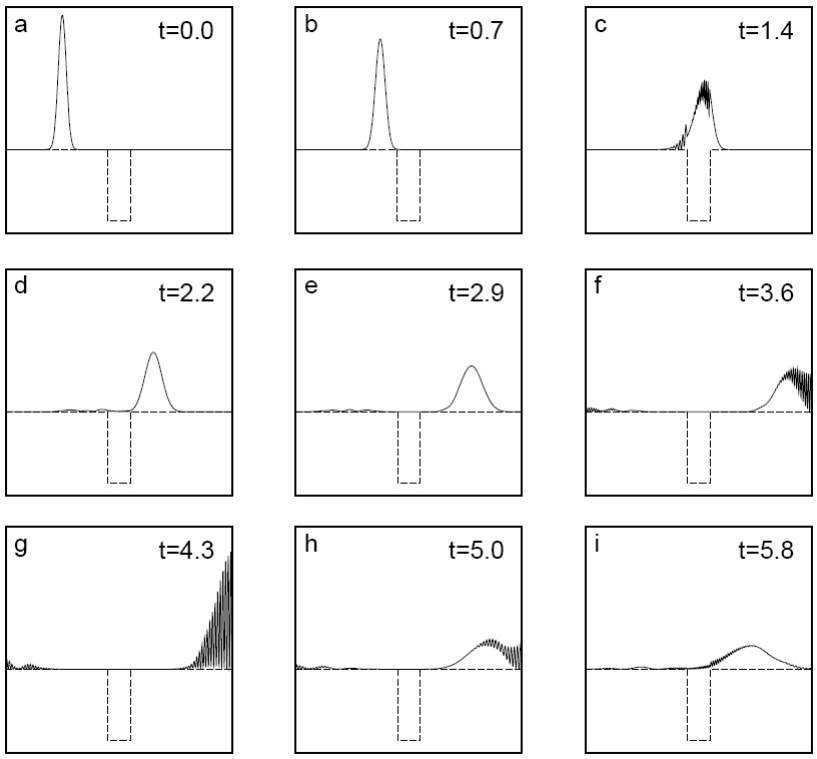

Figure 3.1: Graphics of ψ^2 vs x, for the scattering of the wave packet (4.34). The initial conditions are $x_0 = -10, x_b = 2$, $t_0 = 0$ and $p_0 = 7$. The left and right borders of the domain are $x_{min} = -20$ and $x_{max} = 20$ respectively. The size of every lattice in the grid is $\Delta x = 0.04$ with $N = 1000$ discrete lattices in all the spatial domain and the time step is $\Delta t = 0.002$. With the given parameters the matrix elements are calculated from Eq. (3.15). The given times are for the variable $t = t_0 + n\Delta t$.

3.1.3 Particle Scattered from a Finite Square barrier

As a second example, we define the potential function as

$$V(x) = \begin{cases} p_0^2/2, & -x_b < x < x_b; \\ 0, & \text{otherwise.} \end{cases} \tag{3.26}$$

This is a potential barrier whose height is equal to the average energy $p_0^2/2$ of the Gaussian wave–packet. In Fig 3.2 we show the Gaussian wave–packet scattering from the square barrier (3.26).

Also in this case there exists a strong back reflection effect due to the Dirichlet boundary conditions, however we have a new ingredient in the dynamic behavior of the wave packet and is a kind of resonance. A fraction of the wave packet is captured by the barrier and remains

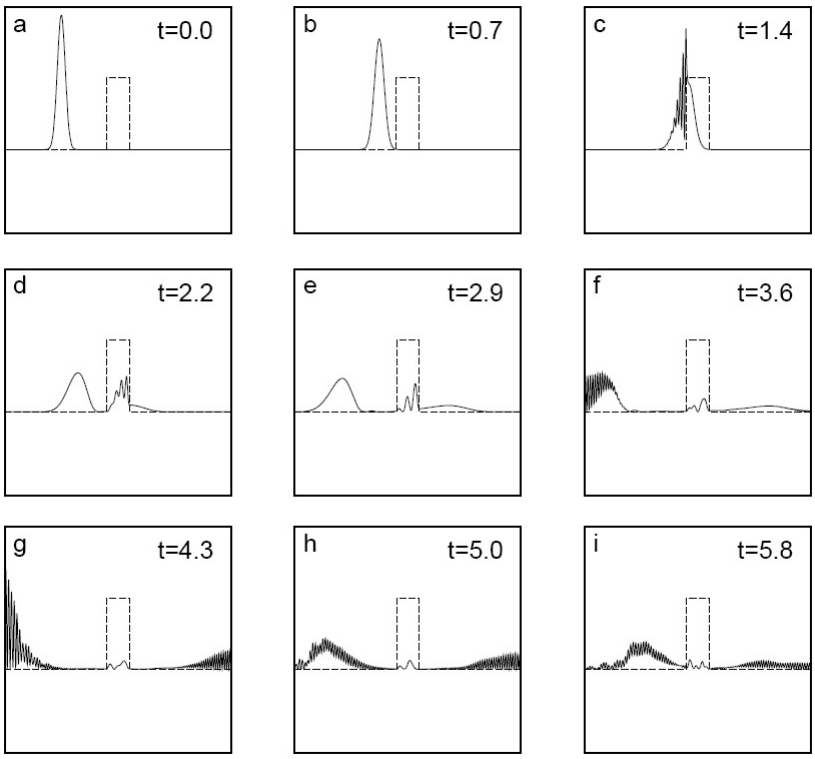

Figure 3.2: Graphics of $|\psi|^2 =$ vs x, for the scattering of the wave packet (4.34). The same parameters as in Fig. 3.1.

trapped for a period which is longer than the time of transmission through the barrier. The captured piece of wave packet bounces back and forth between the barrier walls with a small amount of probability escaping in each collision till the entire packet escapes. Such dynamical behavior is not desirable in this numerical scheme when one tries to calculate transmission and/or reflection coefficients, because sooner or later the transmitted and reflected waves will interfere. Yet, should be pointed out that the above-described method can be coupled in a natural way with an absorbing boundary condition at an artificial boundary to simulate the solution in an open domain.

3.2 Method with Absorbing Boundary Conditions

The numerical solutions of the time–dependent Schrödinger equation, provide us insight in to the dynamics of quantum mechanical systems. However, as was discussed in the previous section, in practical calculations the area of computation must be limited to a finite grid because of the finite capacity of the computer memories. This finite grid produces undesirable reflections at the artificial boundaries of the area of computation. To minimize this artificial

effect, we implement in the present chapter the so called absorbing boundary conditions. These are local boundary conditions that approximate the one way wave equation of a wave function [43].

Let us set the following equation as the starting point of the discussion

$$i\hbar\frac{\partial}{\partial t}\psi(x,t) = \left(-\frac{\hbar^2}{2m^*}\frac{\partial^2}{\partial x^2} + V(x)\right)\psi(x,t). \tag{3.27}$$

In order to obtain the formulas for the absorbing boundary conditions, we consider the special solutions $\psi(x,t) = \exp(-i(\omega t - kx))$, these are states of definite energy E which satisfy the dispersion relation,

$$\hbar^2 k^2 = 2m^*(\hbar\omega - V), \tag{3.28}$$

which is obtained by substituting $E = \hbar\omega$ and $p = \hbar k$ into $p^2 = 2m^*(E - V)$. In terms of $\hbar k$ we get

$$\hbar k = \pm\sqrt{2m^*(\hbar\omega - V)}. \tag{3.29}$$

In this equation plus and minus signs means the right-going and left-going waves respectively. Thus the absorbing boundary conditions must be designed to satisfy the dispersion relation given by the plus signed Eq.(3.29) at the boundary x_{max} and the minus signed at the boundary x_{min}. These are the so called one-way wave equations for the wave function. However, function (3.29) is not rational and cannot be converted into a partial differential equation, therefore we approximate this relation to

$$\hbar k = g_1(\hbar\omega - V) + g_2\,, \tag{3.30}$$

with

$$g_1 = \pm\frac{\sqrt{2m^*\alpha_2} - \sqrt{2m^*\alpha_1}}{\alpha_2 - \alpha_1}, \quad g_2 = \pm\frac{\alpha_2\sqrt{2m^*\alpha_1} - \alpha_1\sqrt{2m^*\alpha_2}}{\alpha_2 - \alpha_1}\,. \tag{3.31}$$

Equation (3.31) is a straight line which crosses Eq. (3.29) at $\hbar\omega - V = \alpha_{1,2}$ (see Fig. 3.3). The correspondence of $\partial/\partial t \Leftrightarrow -i\omega$ and $\partial/\partial x \Leftrightarrow ik$ leads us to rewrite Eq. (3.31) into a partial differential equation of

$$i\hbar\frac{\partial}{\partial t}\psi(x,t) = \left(-i\hbar\frac{1}{g_1\partial x} + V - \frac{g_2}{g_1}\right)\psi(x,t). \tag{3.32}$$

Now we outline how to incorporate the ABC into the lattice representation of the wave function (with $\hbar = m^* = 1$). The idea is to replace the differential equation for the boundary components ψ_N^n and ψ_1^n of the state vector $\vec{\psi}^n$. As was discussed in [31], in order to obtain an accurate expression for the derivative at the borders of the grid is convenient to introduce an intermediate point $\bar{x}$ between the last two points of every side of the grid, then for example, at the right hand side the wave function must be replaced by

$$\psi(\bar{x},t) \simeq \frac{1}{2}[\psi(x_N,t) + \psi(x_{N-1},t)]. \tag{3.33}$$

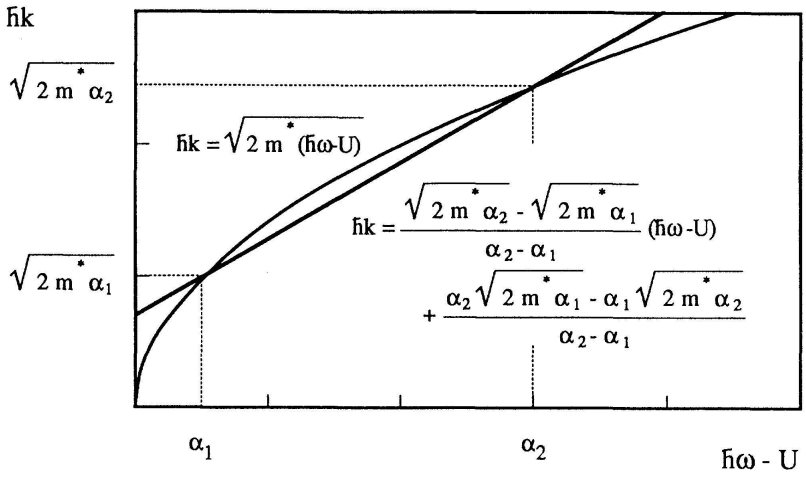

Figure 3.3: The dispersion relation and its first order approximation for the right going wave.

In the grid representation, the finite-difference equation for the right and left sides reads

$$\begin{aligned}\frac{i}{2\Delta t}(\psi_N^{n+1}+\psi_{N-1}^{n+1}-\psi_N^n-\psi_{N-1}^n) &= \frac{-i}{g_1\Delta x}(\psi_N^n-\psi_{N-1}^n)\\ &+ \frac{1}{2}\left(V-\frac{g_2}{g_1}\right)(\psi_N^n+\psi_{N-1}^n)\,, \end{aligned} \tag{3.34}$$

and

$$\begin{aligned}\frac{i}{2\Delta t}(\psi_2^{n+1}+\psi_1^{n+1}-\psi_2^n-\psi_1^n) &= \frac{i}{g_1\Delta x}(\psi_2^n-\psi_1^n)\\ &+ \frac{1}{2}\left(V-\frac{g_2}{g_1}\right)(\psi_2^n+\psi_1^n)\,, \end{aligned} \tag{3.35}$$

respectively. Where we have done the changes in the signs for g_1 and g_2, taking in to account the direction of propagation of the wave in every side of the grid. The equations (3.34,3.35) allows for a straightforward incorporation into the matrix representation Eq. (3.12,3.13). The new matrices $\mathbf{D}_{1,2}$ are given by

$$\mathbf{D}_1 = \begin{pmatrix} \eta_4 & \eta_3 & & & & \\ \alpha & \gamma_2^n & \alpha & & & \\ & \alpha & \gamma_3^n & \alpha & & \\ & & \ddots & \ddots & \ddots & \\ & & & \alpha & \gamma_{N-1}^n & \alpha \\ & & & & \eta_3 & \eta_4 \end{pmatrix} \tag{3.36}$$

$$\mathbf{D}_2 = \begin{pmatrix} \eta_2 & \eta_1 & & & & \\ -\alpha & \xi_2^n & -\alpha & & & \\ & -\alpha & \xi_3^n & -\alpha & & \\ & & \ddots & \ddots & \ddots & \\ & & & -\alpha & \xi_{N-1}^n & -\alpha \\ & & & & \eta_1 & \eta_2 \end{pmatrix} \tag{3.37}$$

with

$$\eta_1 \equiv \eta_1 \equiv \frac{i}{2\Delta t} \tag{3.38}$$

$$\eta_3 \equiv \frac{i}{2\Delta t} + \frac{i}{g_1 \Delta x} + \frac{1}{2}\left(V - \frac{g_2}{g_1}\right) \tag{3.39}$$

$$\eta_4 \equiv \frac{i}{2\Delta t} - \frac{i}{g_1 \Delta x} + \frac{1}{2}\left(V - \frac{g_2}{g_1}\right). \tag{3.40}$$

The main cause of artificial back reflection for plane waves in the presence of the above boundary conditions comes from the approximate nature of the finite difference evaluation. Clearly, these approximations becomes better with decreasing the grid spacing Δx.

Due to the non–symmetric character of the new matrices, we have to calculate one by one the elements in Eq. (3.17) and not just half of them as in Eq. (3.20). In the present case, the elements in the matrix (3.16) are given by $a_1 = a_N = \eta_2$, $b_1 = c_{N-1} = \eta_1$, $b_j = -\alpha$ for $j = 2, ..., N-1$ and $c_j = -\alpha$ for $j = 1, ..., N-2$. The elements in $(\mathbf{D}_2)_{ij}^{-1} = d_{ij}$ are given by

$$\begin{aligned}
&d_{11} = \phi_2/\theta_N, \\
&d_{1j} = (-1)^{1+j}\eta_2(-\alpha)^{|j-2|}\phi_{j+1}/\theta_N, \quad \text{for} \quad j = 2, ..., N \\
&d_{ij} = (-1)^{i+j}(-\alpha)^{|j-i|}\theta_{i-1}\phi_{j+1}/\theta_N, \quad \text{for} \quad i, j = 2, ..., N \quad \text{with} \quad i \le j \\
&d_{ij} = (-1)^{i+j}(-\alpha)^{|i-j|}\theta_{j-1}\phi_{i+1}/\theta_N, \quad \text{for} \quad i = 2, ..., N-1,\ j = 1, ..., N \quad \text{with} \quad i > j \\
&d_{Nj} = (-1)^{N+j}\eta_1(-\alpha)^{|N-j-1|}\theta_{j-1}/\theta_N, \quad \text{for} \quad j = 1, ..., N-1.
\end{aligned}$$

with

$$\begin{aligned}
&\theta_0 = 1, \\
&\theta_1 = \eta_2, \\
&\theta_2 = \xi_2\eta_2 + \alpha\eta_1, \\
&\theta_i = \xi_i\theta_{i-1} - \alpha^2\theta_{i-2}, \quad \text{for} \quad i = 3, ..., N-1 \\
&\theta_N = \eta_2\theta_{N-1} + \alpha\eta_1\theta_{N-2}
\end{aligned}$$

and

$$
\begin{aligned}
&\phi_{N+1} = 1, \\
&\phi_N = \eta_2, \\
&\phi_{N-1} = \xi_{N-1}\eta_2 + \alpha\eta_1, \\
&\phi_i = \xi_i\phi_{i+1} - \alpha^2\phi_{i+2}, \quad \text{for} \quad i = N-2, ..., 2 \\
&\phi_1 = \eta_2\phi_2 + \alpha\eta_1\phi_3.
\end{aligned}
$$

On the other hand the non-symmetric character of the matrices $\mathbf{D}_{1,2}$ does not let us to write the matrix product $\mathbf{E} = \mathbf{D}_2^{-1}\mathbf{D}_1$ as simple as in Eq. (3.11). The new components of the product are

$$
\begin{aligned}
&E_{i1} = \eta_4 d_{i1} + \alpha d_{i2}, \quad \text{for} \quad i = 1, ..., N \\
&E_{i2} = \eta_3 d_{i1} + \gamma_2 d_{i2} + \alpha d_{i3}, \quad \text{for} \quad i = 1, ..., N \\
&E_{ij} = \alpha d_{ij-1} + \gamma_j d_{ij} + \alpha d_{ij+1} \quad \text{for} \quad i = 1, ..., N, j = 3, ..., N-2 \\
&E_{iN-1} = \alpha d_{iN-2} + \gamma_{N-1} d_{iN-1} + \eta_3 d_{iN} \quad \text{for} \quad i = 1, ..., N \\
&E_{iN} = \alpha d_{iN-1} + \eta_4 d_{iN} \quad \text{for} \quad i = 1, ..., N
\end{aligned}
$$

It should be noted that the parameters in Eq. (3.15) are the same, but now these parameters are defined between 2 and $N-1$. In the next sections we apply the method to the same specifics systems considered in the previous section in order to observe the effect of the ABC.

3.2.1 Particle Scattered from a Finite Square Potential Well

In order to observe the effect of the ABC in the borders of the grid, we use the same examples given before for the time–independent potentials. In this example we consider the square well and the Gaussian wave–packet

$$
\psi(x,0) = \sqrt[4]{\frac{1}{\pi}} \exp\left[ip_0(x-x_0) - \frac{(x-x_0)^2}{2}\right], \tag{3.41}
$$

as test particle. The potential function is defined as in the previous example,

$$
V(x) = \begin{cases} -p_0^2/2, & -x_\mathrm{b} < x < x_\mathrm{b}; \\ 0, & \text{otherwise.} \end{cases} \tag{3.42}
$$

In Fig 3.4, we show a wave packet scattering off a square well.

Comparing Figs 3.1 and 3.4 we can see that panels (a-e) are identical but the following panels show us a very different dynamical behavior owing the presence or not of the ABC. As can be seen from the Fig. 3.4, the boundary conditions effectively reduce the non–physical reflections of the impinging wave packet at the boundary of the computation area, letting the wave packet behaves like inside an infinite large grid.

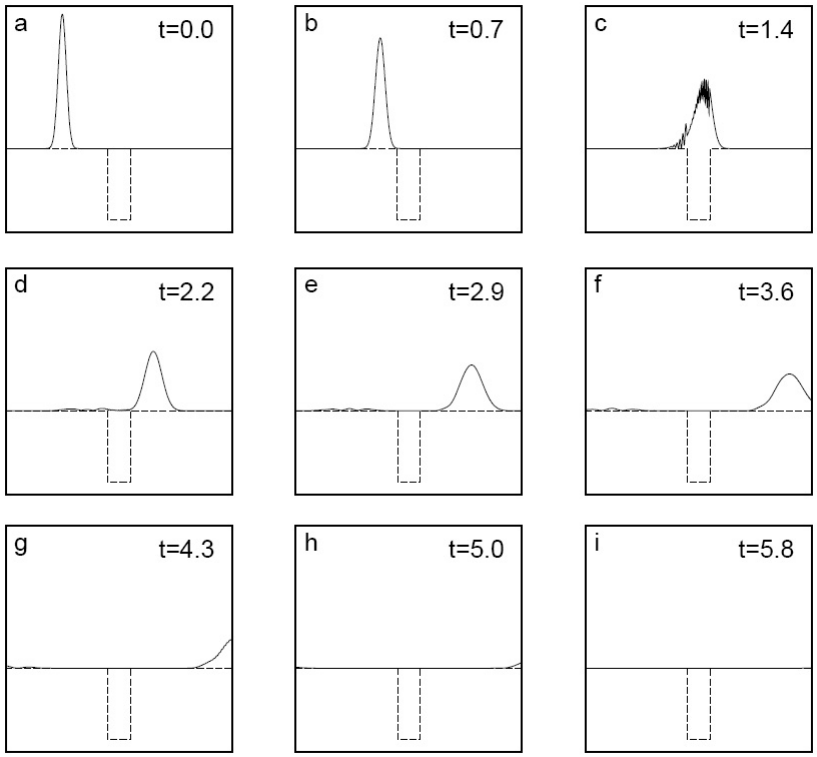

Figure 3.4: Graphics of $|\psi|^2$ vs x, for the scattering of the wave packet (4.34) in the presence of ABC. In this case we choose $\alpha_1 = 24$ and $\alpha_2 = 25$, the other initial conditions and parameters are the same as in Fig 3.1

3.2.2 Particle Scattered from a Finite Square barrier

In this example we consider the square barrier and the Gaussian wave–packet (4.34) as test particle. The potential function is defined as

$$V(x) = \begin{cases} p_0^2/2, & -x_\mathrm{b} < x < x_\mathrm{b}; \\ 0, & \text{otherwise.} \end{cases} \tag{3.43}$$

In Fig 3.5 we show a wave packet scattering off a square barrier.

Also in this case there is no back reflection effect, and the resonance effect could be better observed because we do not have interference due to the reflection of wave packet in the borders. The last panel (panel (i) in Fig. 3.5), remains with a piece of wave packet in the right side, it was considered as the last one in order to observe the remaining resonance. In the numerical simulation, a few seconds after the given time for the last panel, we do not observe any piece of wave packet inside the numerical region. The clear presentation of the resonances let us study its dynamical evolution in a detailed way, but should be noted that

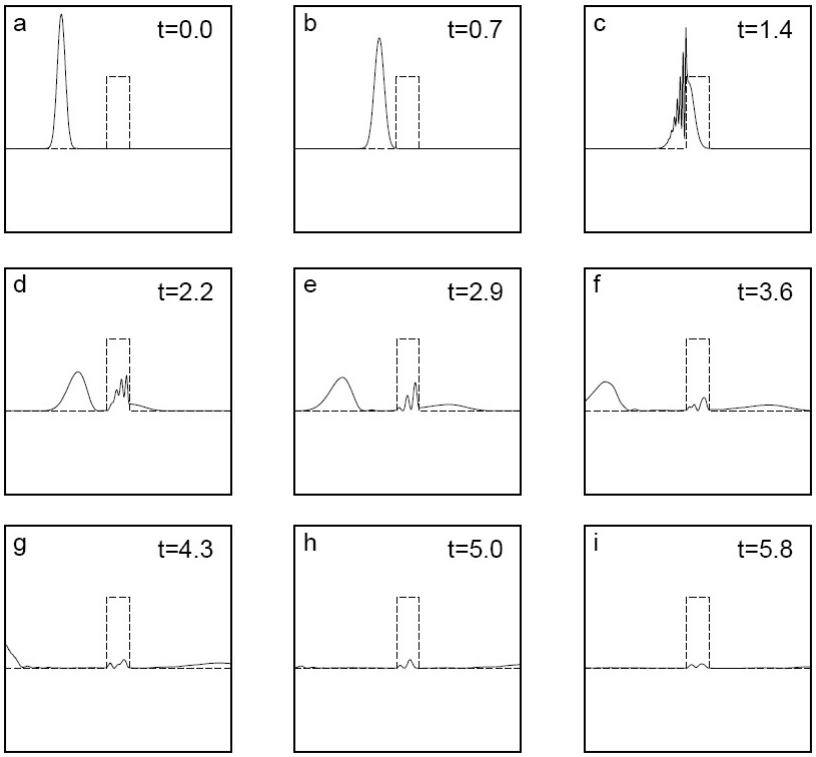

Figure 3.5: Graphics of $|\psi|^2$ vs x, for the scattering of the wave packet (4.34). The same parameters as in Fig. 3.4.

still being hard to study transmission and reflection coefficients in such a system without a largest grid.

3.3 Method with Absorbing Boundary Conditions and Source Term

As a last case to prove the validity and effectiveness of our simplified method, we consider the presence of a source term. The equation of motion now reads

$$i\frac{\partial}{\partial t}\psi(x,t) = H(x,t)\psi(x,t) + S(t)\exp(-i\omega t)\delta(x)\,, \tag{3.44}$$

where $S(t) = S_0[1-\exp(-t/\Delta T)]$. This function provides a smooth evolution of the source term toward the desired final value $S(t\to\infty) = S_0$. In order to have an analytical result to compare the numerical results, we consider the stationary solutions of Eq. (3.44) for the particular case $V(x) = 0$ with $S(t) = S_0$. Introducing the Fourier transformed wave function

$\tilde{\psi}(q,t) = \int \exp(iqx)\psi(x,t)dq$ and considering the previous conditions, the Eq. (3.44) takes the form

$$\left(i\frac{\partial}{\partial t} - \frac{\hbar^2 q^2}{2m}\right)\tilde{\psi}(q,t) = S_0 \exp(-i\omega t). \tag{3.45}$$

This equation admits solutions of the form

$$\tilde{\psi}(q,t) = \frac{2S_0}{k^2 - q^2}\exp(-i\omega t)\,,$$

where $k^2 = 2\omega$. Transforming back to the configuration space, the solution is given by

$$\psi(x,t) = \frac{S_0}{ik}\exp(ik|x|)\exp(-i\omega t). \tag{3.46}$$

It means that the source emits in both direction a monochromatic wave (3.46).

As was showed in [31], working with a grid representation of the wave function, it is convenient to approximate the δ function by

$$R(x) = \frac{1}{\Delta x}[\Theta(x + \Delta x/2) - \Theta(x - \Delta x/2)], \tag{3.47}$$

where Θ is the Heaviside step function. With this approximation, the error scales quadratically with the size of the grid Δx and becomes negligible for reasonable small values of Δx. The implementation of the source term at position $x_{j'}$ in the grid representation reads as

$$S_j^n = S(t_n)\exp(-i\omega t_n)\delta_{j,j'}$$

where $\delta_{j,j'} = 1$ if $j = j'$ and 0 otherwise. In the presence of the source term the Eq. (3.9) is given by

$$\mathbf{D}_2\vec{\psi}^{n+1} + \vec{b}^n = \mathbf{D}_1\vec{\psi}^n \Leftrightarrow \vec{\psi}^{n+1} = \mathbf{D}_2^{-1}(\mathbf{D}_1\vec{\psi}^n - \vec{b}^n), \tag{3.48}$$

where the components of the vector $\vec{b}^n$ are

$$b_j^n = \frac{i\Delta t}{2}(S_{j'}^n + S_{j'}^{n+1})\delta_{j,j'}. \tag{3.49}$$

The numerical implementation is the same as in the previous section with the only difference that we have to construct the new vector $\vec{b}$ and subtracts it as was indicated in Eq. (3.48), i.e. we can use the results given above for the analytical inverse $\mathbf{D}_2^{-1}$ and for the product $\mathbf{E} = \mathbf{D}_2^{-1}\mathbf{D}_1$.

3.3.1 Plane Waves with Constant Amplitude

As a first example we consider the case $V(x) = 0$ and $S(t) = S_0$ in which the exact solution was given as

$$\psi(x,t) = \frac{S_0}{ik}\exp(ik|x|)\exp(-i\omega t). \tag{3.50}$$

In Fig. 3.6 we compare the exact Eq. (3.50) and the numerical results for this case. We find excellent agreement between the numerical and exact results in all cases considered. It is worth to mentioning that after 5000 iterations the method still being very stable, and also should be noted the behavior of the Absorbing Boundary Conditions, which regardless that the source is filling the numerical region the numerical evolution simulates an open domain.

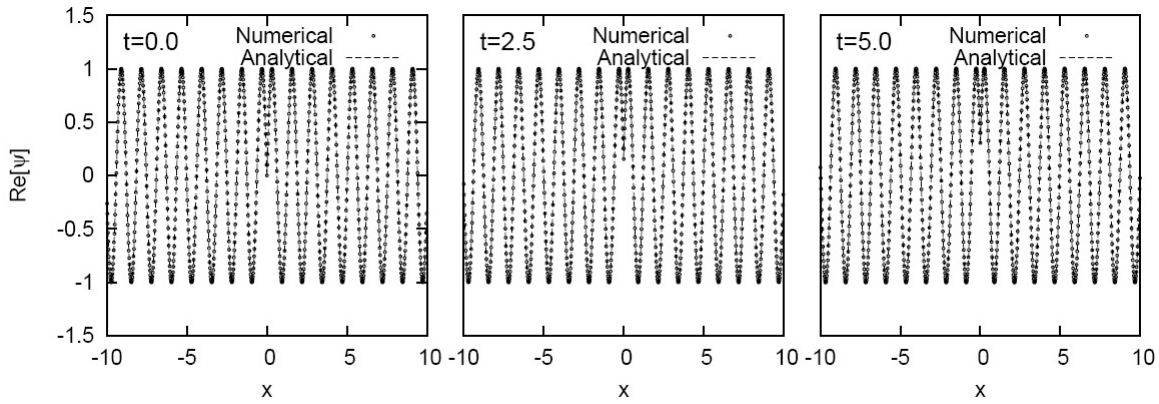

Figure 3.6: Graphics of $Re[\psi]$ vs x, for the analytical (dashed line) and numerical (dots) solution to the Schrödinger equation with source term. The initial conditions are $x_0 = 0$, $t_0 = 0$, $\alpha_1 = 12$, $\alpha_2 = 13$, $S_0 = 5$, $\omega = (p_0 - g_2)/g_1$ and $p_0 = 5$. The left and right borders of the domain are $x_{min} = -10$ and $x_{max} = 10$ respectively. The size of every lattice in the grid is $\Delta x = 0.02$ with $N = 1000$ discrete lattices in all the spatial domain and the time step is $\Delta t = 0.001$. With the given parameters the matrix elements for (3.36) and (3.37) are calculated from Eq. (3.15). The given times are for the variable $t = t_0 + n\Delta t$.

3.3.2 Plane Waves with Time–Dependent Amplitude

The present case is of physical interest because the idea of an initially empty waveguide that is gradually filled with matter waves corresponds to the experimental realization of a reservoir located at $x = x_0$. The time evolution of the real part of the wave function and the probability density during the increase of the source amplitude is displayed in Figs. 3.7 and 3.8.

As was expected for propagation times $t \gg \Delta t$ the calculation converges toward a flat density, that corresponds to the stationary plane waves at the source amplitude $S = S_0$. The most important result, is that the Figs. 3.7 and 3.8 illustrate that the source emits a plane wave like a solution of the form $A(x,t)\exp[-i\omega t + ik(x,t)x]$, where $A(x,t)$ and $k(x,t)$ vary slowly in time and position. The ABC are well behaved, after 12000 iterations the probability still conserved (see last panel in Fig. 3.8). This result let us to consider the possibility to use the method for the case of time–dependent potentials in which the k parameter will be varied by the interaction between the plane wave and the potential.

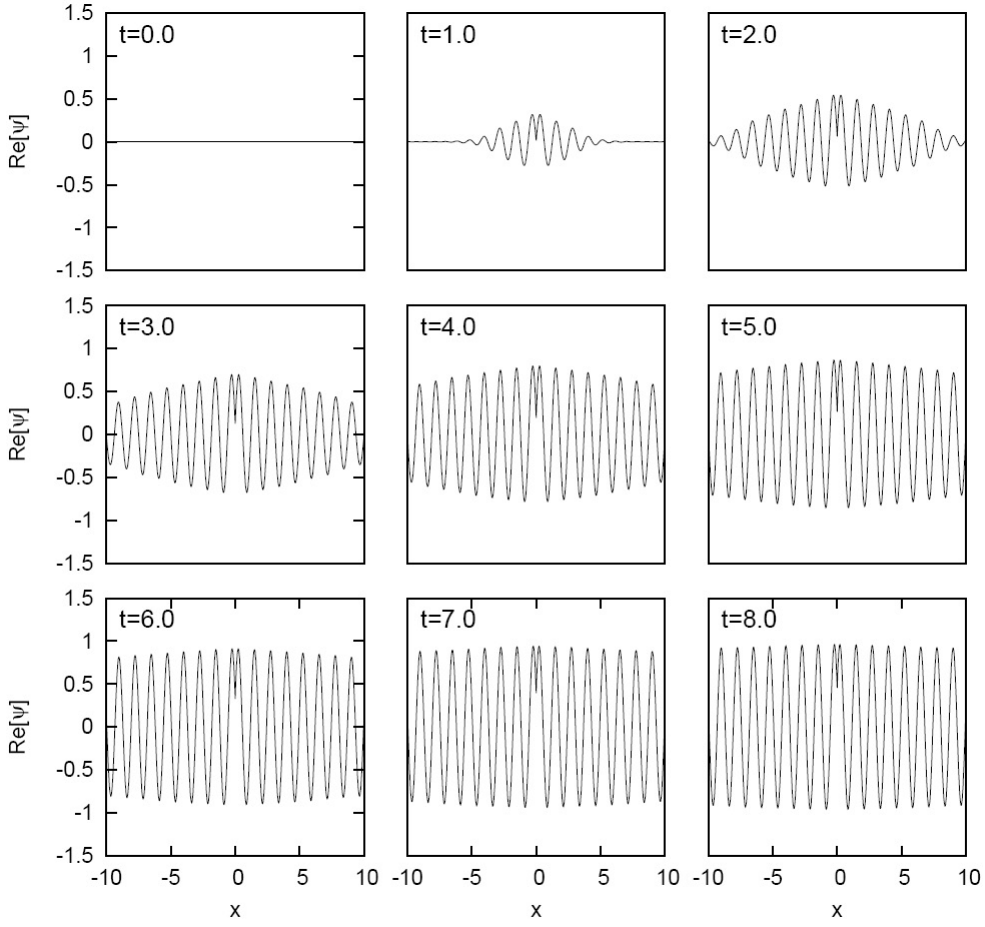

Figure 3.7: Graphics of $Re[\psi]$ vs x, for the numerical solution to the Schrödinger equation with time–dependent source term. The initial conditions are $x_0 = 0$, $t_0 = 0$, $\alpha_1 = 12$ $\alpha_2 = 13$, $S_0 = 5$, $\omega = (p_0 - g_2)/g_1$, $\Delta T = \omega$ and $p_0 = 5$. The left and right borders of the domain are $x_{min} = -10$ and $x_{max} = 10$ respectively. The size of every lattice in the grid is $\Delta x = 0.02$ with $N = 1000$ discrete lattices in all the spatial domain and the time step is $\Delta t = 0.001$. With the given parameters the matrix elements for (3.36) and (3.37) are calculated from Eq. (3.15). The given times are for the variable $t = t_0 + n\Delta t$.

3.4 Summary

We have described a numerical integration method for the time–dependent Schrödinger equation with an without source terms. In particular, we consider the case of scattering systems, in which the Dirichlet boundary conditions produces undesired reflections. To solve this problem we have introduced absorbing boundary conditions (ABC) into this integration scheme. The numerical integration was done using the Crank-Nicholson method together with a Cayley's form for the finite-difference representation of evolution operator which produces an

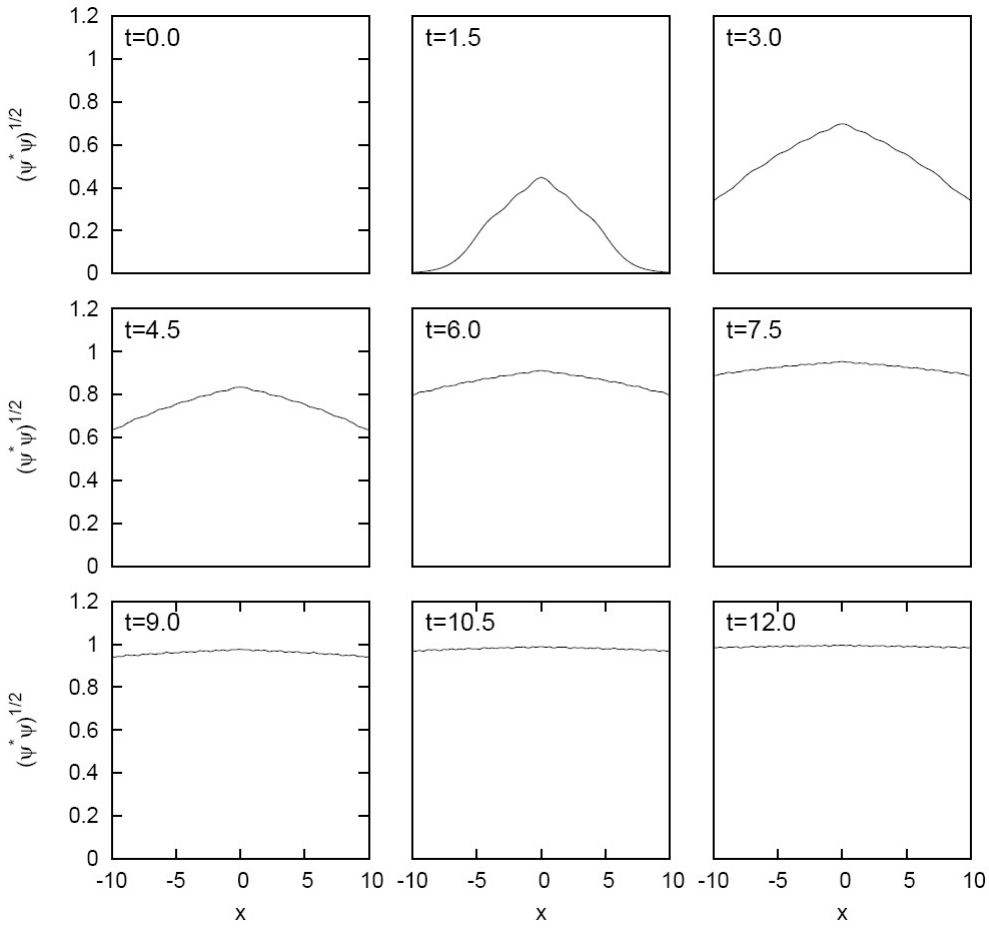

Figure 3.8: Graphics of $|\psi|$ vs. x, for the numerical solution to the Schrödinger equation with time–dependent source term. The initial conditions and parameters are the same as in Fig. 3.7.

stable, unitary, and second-order accurate in space and time method. On replacing the Hamiltonian by its finite-difference approximation in x, we have reduced the problem to a complex tridiagonal system. We have simplified the numerical scheme inverting by hand the matrices by means of the Usmani's formula for Jacobian matrices. The analytical inversion of the matrices decrease the computational effort. This is desirable for the case of time–dependent potentials, in which the matrices vary in every time step as we will see in the next chapter. We ended this chapter by comparing the results our modified numerical method, with the exact solution for the Schrödinger equation with source term, where we find an excellent level of agreement.

4 Quantum Spin Pump

In this chapter we describe the quantum stroboscopic evolution of an initial state in the presence of a kicked magnetic field. As a first approach, we consider the case of a kicked magnetic field with a single component, $\vec{B} = (0, 0, B_z)$. With the aim of gain some insight about the behavior of every spin, we calculate the transmission and reflection probabilities as a function of the period of the kicks τ. We show that the multiphoton absorption/emission process, $\Delta E = n\hbar\omega$, inherent to every time periodic system, allows us to calculate the transmission probabilities and hence the currents in terms of the Floquet channels. We shall briefly present the plots of the evolution operator in momentum representation, which, from a qualitative point of view, give us information about the possibility to get directed transport as an analog to the transmission/reflection plots of the classical case. To end this section, we solve the general problem with two perpendicular kicked magnetic fields, $\vec{B} = (0, B_y, B_z)$. Our numerical results, demonstrate that the breaking of spatio-temporal symmetries gives rise to particle and spin currents, which can be modulated by the pumping frequency or the external magnetic flux. For certain set of parameters the pumped spin current can generate even pure spin current.

4.1 The Floquet Operator

The dynamical evolution of the quantum system is governed by the Schrödinger equation,

$$i\hbar\frac{\partial}{\partial t}|\psi(t)\rangle = H(t)|\psi(t)\rangle, \tag{4.1}$$

where H is the Hamiltonian describing the system. Formally, the solution of (4.1) is

$$|\psi(t)\rangle = \mathcal{T}\exp\left(-\frac{i}{\hbar}\int_0^t H(t')dt'\right)|\psi(0)\rangle \equiv U(t,0)|\psi(0)\rangle, \tag{4.2}$$

where $\mathcal{T}$ is the time ordering operator and $U(t,0)$, is the unitary time–evolution operator. With correct time ordering, it becomes evident that the relation $U(t,0) = U(t,s)U(s,0)$ holds and due to the unitary nature of the time evolution, $U(t,s) = U(t,0)U^{\dagger}(s,0)$. In particular,

for the case of kicked (time periodic) potentials

$$H(x,t) = H_0(x) + V(x)\sum_{n=0}^{\infty}\delta(n\tau - t), \tag{4.3}$$

where H_0 is the time-independent Hamiltonian and $V(x)$ is an operator describing the perturbation; the solution to the Schrödinger equation at times $n\tau$, is given by

$$|\psi(n\tau)\rangle = F^n|\psi(0)\rangle, \tag{4.4}$$

where F is called the Floquet operator, which is simply the time evolution operator U over a single kick period τ, $F = U(n\tau, n-1\tau)$.

The time evolution over one period for the Hamiltonian (4.3) can be written as

$$F = \exp\left(-\frac{i}{\hbar}\int_{\epsilon}^{\tau-\epsilon} H(t)dt\right)\exp\left(-\frac{i}{\hbar}\int_{\tau-\epsilon}^{\tau+\epsilon} H(t)dt\right). \tag{4.5}$$

The first factor, for time $\epsilon < t < \tau - \epsilon$, is trivial because the delta function in (4.3) is not acting, $H(t) = H_0$ is independent of time and the system evolves freely via the time-evolution operator

$$U_{\text{free}} = \exp\left(-\frac{i}{\hbar}H_0\tau\right). \tag{4.6}$$

The second factor is over an infinitesimal time period 2ϵ when the delta function kick is acting. Over this infinitesimally short period of time, the influence from the time–independent Hamiltonian H_0 is zero and the system instantaneously evolves via the operator

$$U_{\text{kick}} = \exp\left(-\frac{i}{\hbar}V\right). \tag{4.7}$$

Recombining these two parts of the evolution, the operator describing the evolution of the system from just before one kick to just before the next one is

$$F = \exp\left(-\frac{i}{\hbar}H_0\tau\right)\exp\left(-\frac{i}{\hbar}V\right). \tag{4.8}$$

Once the Floquet operator has been obtained, numerical investigations of the system become far more tractable and the stroboscopic picture of the evolution of the quantum system can be expressed as

$$|\psi_{n+1}\rangle = \exp\left(-\frac{i}{\hbar}H_0\tau\right)\exp\left(-\frac{i}{\hbar}V\right)|\psi_n\rangle. \tag{4.9}$$

Here, for simplicity we have changed the notation $|\psi_{n+1}\rangle \equiv |\psi(\tau(n+1))\rangle$ and $|\psi_n\rangle \equiv |\psi(\tau n)\rangle$.

The central rôle that the Floquet operator plays in the work presented in this thesis warrants a detailed introduction, but for more details and some simple examples of the Floquet operator we refer the reader to [44].

4.1.1 Numerical Evaluation of the Propagator in the Position Representation

The dynamics of the quantum system, can be formulated as a discretization of the integral form of the quantum map (4.9) in the position representation,

$$\langle x|\psi_{n+1}\rangle = \int\int \langle x|U_{\text{free}}|x''\rangle\langle x''|U_{\text{kick}}|x'\rangle\langle x'|\psi_n\rangle dx'dx'' \,. \tag{4.10}$$

The position representation of the free-particle propagator, can be calculated analytically and is given by

$$K(x,\tau;x'',0) = \langle x|U_{\text{free}}|x''\rangle = U_{\text{free}}(x,x'') = \sqrt{\frac{m}{2\pi i\hbar\tau}}\exp\left(\frac{i}{\hbar}\frac{m(x-x'')^2}{2\tau}\right). \tag{4.11}$$

The Eq. (4.10) could be written as

$$\begin{aligned}\psi_{n+1}(x) &= \int\int U_{\text{free}}(x,x'')U_{\text{kick}}(x',x'')\delta(x'-x'')\psi_n(x')dx'dx'' \\ &= \int U_{\text{free}}(x,x')U_{\text{kick}}(x')\psi_n(x')dx' \,. \end{aligned}\tag{4.12}$$

Using the spatial discretization, the integral can be approximated by

$$\int f(x)dx \approx \sum_{j=1}^{N} f(x_j)\Delta x \,, \tag{4.13}$$

using (4.11) and (4.13), the expression (4.12) is given by

$$\psi_{n+1}(x_j) \approx \sqrt{\frac{m}{2\pi i\hbar\tau}}\sum_{j'=1}^{N}\exp\left(\frac{i}{\hbar}\frac{m(x_j-x_{j'})^2}{2\tau}\right)\exp\left(-\frac{i}{\hbar}V(x_{j'})\right)\psi_n(x_{j'})\Delta x', \tag{4.14}$$

with $\Delta x' = (x_{\max} - x_{\min})/N$. Here $x_{\max}$ and $x_{\min}$ are the boundaries of the finite grid, N the number of lattices sites, $x_{j'} = x_{\min} + j'\Delta x'$ with $j' = 0,\ldots,N$ and $x_N = x_{\max}$.

The map (4.14) is more concisely denoted in vectorial form

$$\vec{\psi}_{n+1} = F^{(\text{pr})}\vec{\psi}_n$$

with the vectors

$$\vec{\psi}_n = \begin{pmatrix} \psi_n(x_1) \\ \vdots \\ \psi_n(x_N) \end{pmatrix}, \tag{4.15}$$

and the matrix elements of the Floquet operator in position representation (hereafter $m = 1$)

$$\begin{aligned} F_{jj'}^{(\mathrm{pr})} &= \frac{x_{\max} - x_{\min}}{N} \sqrt{\frac{1}{2\pi i \hbar \tau}} \exp\left(\frac{i}{\hbar} \frac{(x_j - x_{j'})^2}{2\tau}\right) \\ &\quad \times \exp\left(-\frac{i}{\hbar} V(x_{j'})\right), \quad 1 \le j, j' \le N. \end{aligned} \tag{4.16}$$

Note that $F_{jj'}^{(\mathrm{pr})}$, which describes the propagation over a full period of the excitation, is the same for all n, such that it suffices to determine its matrix elements once and store them for repeated use. In order to obtain a numerically stable algorithm, $F_{jj'}^{(\mathrm{pr})}$ must be required to be unitary,

$$\sum_{j'=1}^{N} |F_{jj'}^{(\mathrm{pr})}|^2 = 1 \quad \forall j,$$

it is

$$\frac{(x_{\max} - x_{\min})^2}{N} \approx 2\pi\hbar\tau. \tag{4.17}$$

From the previous discussion, can be concluded that the parameters $x_{\max}, x_{\min}$ and N of the numerical algorithm, on the left hand side of equation (4.17), have to be chosen as specified by the physical parameters $\hbar$ and τ on the right hand side. Note that the kick amplitude does not interfere with the unitarity of $F_{jj'}^{(\mathrm{pr})}$. In addition to the condition (4.17), a periodic boundary condition is implicitly satisfied, which means that the interval must be chosen large enough to allow the discrete mapping to approximate the original. This could be achieved if the wave function decays rapidly enough with reaching out to the boundaries of the interval considered. These two restrictions combined are the reason why the algorithm given by the mapping (4.14) is of limited practical use when we want to study long-time dynamics of spreading states. Conversely, if the dynamics is followed for times not too large, such that the initial wave packets have not spread too much, then equation (4.14) provides a simple and efficient way to evaluate the quantum map, especially for larger values of $\hbar$.

4.1.2 Numerical Evaluation of the Propagator using Finite Differences

Now we use the finite differences approach presented in the previous chapter, which was used to solve the Schrödinger equation for the case of time–independent Hamiltonians in the position representation, where both space and time were discretized in equidistant steps from the beginning. The solution on the interval $[x_{\max}, x_{\min}]$ is constructed at the nodes

$$\begin{aligned} x_{j'} &= x_{\min} + j'\Delta x' \quad \text{with} \quad j' = 0, \ldots, N \\ x_N &= x_{\max}. \end{aligned} \tag{4.18}$$

and the time steps

$$t_n^{(m)} = n\tau + m\Delta t \quad \text{with} \quad m = 0, \ldots, s. \tag{4.19}$$

For simplicity, only the dynamics in the time interval $[n\tau, (n+1)\tau)$ is considered here, such that the subscript n can be avoided. The wave function at site x_j and time $t^{(m)}$ are denoted as

$$\psi_j^m = \langle x_j | \psi(t^m) \rangle.$$

In a first step, U_{kick} is applied to the discretized wave function

$$\psi_j^0 \mapsto \exp\left(-\frac{i}{\hbar} V(x_{j'})\right) \psi_j^0, \tag{4.20}$$

then, the new ψ_j^0 is propagated for a period of time of length τ using the finite differences algorithm that we describe in a very detailed way in the previous chapter. The advantage of this method, is that source terms can be incorporated in the numerical algorithm in a very easy way. A source needs a sink which also cannot be implemented using the numerical evaluation of the Floquet operator in the position representation, but was implemented successfully using the finite differences algorithm as was shown in the previous chapter. The total time evolution of the initial state, can be achieved by taking the initial wave packet ψ_j^0 as the transformed by means of (4.20), and propagating for a period of time τ, the new wave packet is transformed and propagated again and so on.

4.2 The Floquet Operator for Decoupled Spinors

As model we choose a particle with spin$-1/2$ in the presence of a kicked magnetic field. The Hamiltonian for this system is given by

$$H(x,t) = I\frac{\hat{p}^2}{2m_0} - \mu_B \hat{\sigma} \cdot \vec{B}(x,t), \tag{4.21}$$

where for simplicity we choose the magnetic field oriented in the $z-$direction, $\vec{B}(x,t) = B(x,t)\hat{z}$, with

$$B(x,t) = Af(x) \sum_{n=-\infty}^{\infty} \delta(n\tau - t), \tag{4.22}$$

and $f(x)$ given by the envelope function

$$f(x) = \exp\left[\frac{-1}{(a/2)^2 - x^2}\right] \Theta\left[a/2 - |x|\right], \tag{4.23}$$

with $\Theta[x]$, the Heaviside step function. In this case the Schrödinger–Pauli matrix equation can be written as

$$H(x,t)\Psi = -I\frac{\hbar^2}{2m_0}\nabla^2\Psi - \mu_B \sigma_z B\Psi = i\hbar\frac{\partial \Psi}{\partial t}, \tag{4.24}$$

where

$$I = \begin{pmatrix} 1 & 0 \\ 0 & 1 \end{pmatrix}, \sigma_z = \begin{pmatrix} 1 & 0 \\ 0 & -1 \end{pmatrix}, \tag{4.25}$$

and $\Psi = \Psi(x, y, z, t)$ is the two component spinor

$$\Psi = \begin{pmatrix} \psi_+ \\ \psi_- \end{pmatrix}. \tag{4.26}$$

The vectorial equation of motion reads as,

$$\frac{-\hbar^2}{2m_0} \begin{pmatrix} \nabla^2\psi_+ \\ \nabla^2\psi_- \end{pmatrix} - \mu_B B \begin{pmatrix} \psi_+ \\ -\psi_- \end{pmatrix} = i\hbar \begin{pmatrix} \partial\psi_+/\partial t \\ \partial\psi_-/\partial t \end{pmatrix}. \tag{4.27}$$

This equation must be satisfied component by component, then, the system of equations to be solved is given by

$$\frac{-\hbar^2}{2m_0}\nabla^2\psi_+ - \mu_B B\psi_+ = i\hbar\frac{\partial\psi_+}{\partial t}, \tag{4.28}$$

$$\frac{-\hbar^2}{2m_0}\nabla^2\psi_- + \mu_B B\psi_- = i\hbar\frac{\partial\psi_-}{\partial t}. \tag{4.29}$$

Each one of the previous equations can be written in the form (4.1),

$$i\hbar\frac{\partial}{\partial t}|\psi_+(t)\rangle = H_+(t)|\psi_+(t)\rangle, \tag{4.30}$$

$$i\hbar\frac{\partial}{\partial t}|\psi_-(t)\rangle = H_-(t)|\psi_-(t)\rangle, \tag{4.31}$$

with

$$H_+(t) = \frac{\hat{p}^2}{2m_0} - \mu_B B = H_0 - V\sum_{n=0}^{\infty}\delta(n\tau - t), \tag{4.32}$$

$$H_-(t) = \frac{\hat{p}^2}{2m_0} + \mu_B B = H_0 + V\sum_{n=0}^{\infty}\delta(n\tau - t), \tag{4.33}$$

and

$$V = \mu_B A \exp\left[\frac{-1}{(a/2)^2 - x^2}\right]\Theta\left[a/2 - |x|\right].$$

Form a physical point of view, the analysis of the case of a single magnetic field, is interesting because permits us to understand and predict some behaviors of the general problem with two perpendicular kicked magnetic fields. In the classical model, the main particularity that produces the spin currents is the first region of the magnetic field, which behaves like a spin down "filter", creating an unbalance between the spins traveling through the second region of magnetic field. The second magnetic field, induces precessions of the

spin in a plane perpendicular to the local direction of the field. Such precession, is in a general sense not restrictive with respect to the spin orientation, producing an oscillatory evolution which in average, is expected to be the same for both spins.

In the classical case the angular momentum rectification was explained in terms of the equation of motion $\ddot{x} = \nabla(\vec{B}\cdot\vec{S})$, which represents an attractive force in the case $\vec{B}$ parallel to $\vec{S}$ and a repulsive force in the case $\vec{B}$ antiparallel to $\vec{S}$ (in this context spin up is understood as a vector $\vec{S}$ aligned with $\vec{B}$). In the quantum case, the spin rectification could be explained in terms of the Hamiltonians (4.32-4.33), which are in a simplified view a potential well and a potential barrier, respectively. For the case of spins up, we have to solve the analog of the quantum mechanical problem of a particle in the presence of a potential well, while for spins down, the quantum mechanical problem to be solved is the analog of a particle in the presence of a potential barrier. However, should be noted that in the particular case under consideration, the repulsion depends on height, width, and on the period of the kicks.

4.2.1 Comparison of the Numerical Methods

In this section we will present a comparison of the numerical methods developed in section 4.1. First of all, we propagate the initial Gaussian wave–packet

$$\psi(x,0) = (1/\pi)^{1/4}\exp[(x-x_0)(ip_0-(x-x_0)/2)] \tag{4.34}$$

for the case $A = 0$ (indistinguishable particles), using the numerical evaluation of the Floquet operator in the position representation and using the Finite differences algorithm with absorbing boundary conditions, together with the exact solution for the time evolution of a free particle [42],

$$\psi(x,t) = \frac{1}{\sqrt{1+it}}\sqrt[4]{\frac{1}{\pi}}\exp\left[i\frac{x^2}{2t}+\frac{(p_0t-x)^2}{2t(i-t)}\right]$$

with the probability density then given by

$$\rho(x,t) = |\psi(x,t)|^2 = \sqrt{\frac{1}{\pi}}\frac{1}{\sqrt{1+t^2}}\exp\left[-\frac{(x-p_0t)^2}{1+t^2}\right].$$

In Fig. 4.1 we plot the probability density in the three cases at times $t = 0, t = 2$ and $t = 4$ with parameters $\tau = 1, p_0 = 5, x_0 = -10$. We can see an excellent agreement between the numerical and the exact solutions.

For the case $A \neq 0$ we cannot compare with an exact result, so we follow comparing the two numerical methods. In Table 4.1, we compute the transmission coefficients, using the numerical evaluation of the Floquet operator in the position representation (F.O) and the Finite Differences algorithm (F.D) for different values of the linear momentum p_0, the amplitude A and the driving period τ. In column 4 of Table 4.1, we show the percentage error between transmission coefficients, computed with the two numerical methods. We can see that the highest error is equal to 0.5%. It should be pointed out that the smallest value used for the driving period was $\tau = 0.8$, this is due to the fact than a smaller value of τ,

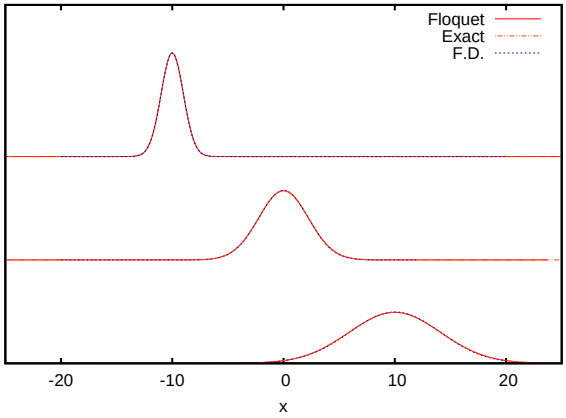

Figure 4.1: Graphics of the probability density for the evolution of a free wave packet (4.34), using the numerical evaluation of the Floquet operator in the position representation, the Finite Differences algorithm (F.D) and the exact solution of the free-particle Schrödinger equation, with parameters $\tau = 1, p_0 = 5, x_0 = -10$ at times $t = 0, t = 2$ and $t = 4$.

implies more points to be taken in the grid and a significant spread out in space of the wave packet, which, is not desirable when one uses the F.O method.

(p_0, A, τ)	T(F.D)	T(F.O)	%E	T+R(F.D)	T+R(F.O)
(5,1,1.0)	0.9990	0.9988	2×10^{-2}	0.9999	0.9997
(4,2,1.0)	0.9888	0.9886	2×10^{-2}	1.0000	1.0000
(4,3,1.0)	0.9766	0.9748	2×10^{-1}	1.0000	1.0000
(4,4,0.9)	0.9963	0.9611	5×10^{-1}	1.0002	0.9999
(2,4,0.8)	0.8184	0.8163	3×10^{-1}	0.9999	1.0001

Table 4.1: Transmission coefficients using the Finite Differences algorithm (column 2) and the numerical evaluation of the Floquet operator in the position representation (column 3) for different values of the linear momentum p_0, the amplitude A and the driving period τ (column 1). In column 4, the percentage error between transmission coefficients with the two numerical methods is computed. In columns 5 and 6, we calculate the total probability density for each method.

Based on the limitations of the F.O. method and the good agreement between the numerical methods in all that follows we consider the F.D. method the most appropriated to compute the transmission coefficients.

In order to gain some insight about the behavior of every one of the spins, in Fig. 4.2 we

plot the transmission and reflection probabilities for every spin as a function of the driving period τ.

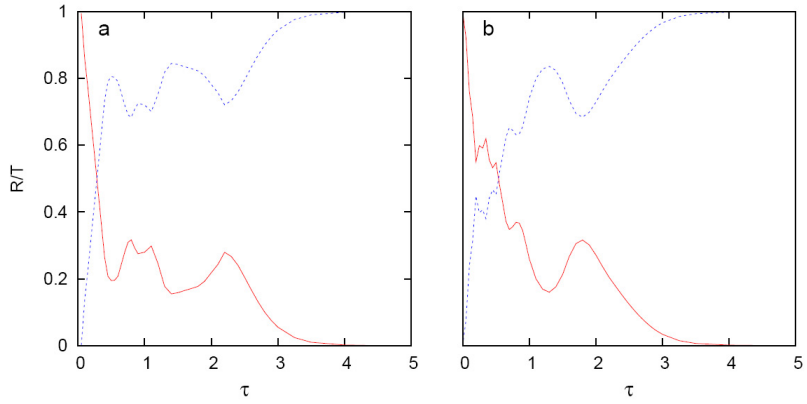

Figure 4.2: Graphics of transmission T (blue line) and reflection R (red line) coefficients vs. the period of the kicks τ, for an incoming spin up (a) and an incoming spin down (b). Each spin state is described by the initial Gaussian wave–packet 4.34. The initial conditions are $x_0 = -10$, $A = 64$, $p_0 = 5$ and $a = 4.04$. The left and right borders of the domain are $x_{\min} = -40$ and $x_{\max} = 40$, respectively. The size of every lattice in the grid is $\Delta x = 0.02$ with $N = 1000$ discrete lattices in all the spatial domain and the time step is $\Delta t = 0.002$.

In Fig. 4.2, we note two extreme behaviors for the transmission coefficients in both cases (spin up and spin down). When $\tau \to 0$, almost all the wave packet tends to be reflected, this is due to the fast and strong driving $A = 64$. For $\tau > 4$, the wave packet tends to be totally transmitted, this could be easily understood because for times longer than $t = 4$, the position of the center and also the tail of the wave packet lies outside of the interaction region. The shifted equi-distribution of probabilities for the spin down ($\tau \approx 0.6$ for $S_\downarrow$ and $\tau \approx 0.3$ for $S_\uparrow$), means that the transmission coefficient grows slowly for the spin down than for the spin up for reasonable short periods in the kicks.

4.2.2 Floquet Channels

From a physical point of view, it is interesting to note that for time–independent scattering systems, the energy is conserved $E_{\text{in}} = E_{\text{out}}$, while for time periodic scattering systems, just the quasi-energy is conserved with the incoming and outgoing energies related by

$$E_{\text{out}} = E_{\text{in}} + l\hbar\omega, \tag{4.35}$$

with $l \in \mathbb{Z}$ and $\omega = 2\pi/\tau$ the driving frequency . Each l in 4.35 is known as a Floquet channel, and represents the net number of photons gained or lost during the scattering process (c.f. [8]-[34] for details). However, in practice not every l corresponds to an allowed Floquet channel, which can be seen from the energy relation (4.35). In the grid representation each $n \in \mathbb{Z}$,

correspond to a position (in position representation), or in other words, each n corresponds to an allowed momentum in the grid (in momentum representation), $p_n = (2\pi\hbar/L)n$, with L the length of the numerical region. Lets assume that the initial momentum is given by $p_m = (2\pi\hbar/L)m$, then equation (4.35) can be written as

$$n = \sqrt{m^2 + \frac{lL^2}{\tau\pi}} \quad \text{using} \quad \hbar = 1. \tag{4.36}$$

It means, that l is an allowed Floquet channel if $l \in \mathbb{Z}$ evaluated in Eq. (4.36), produces $n \in \mathbb{Z}$. In Fig 4.3 we plot l vs. n, in order to observe that just a few l's produces n integers, i.e. just a small number of l's are allowed.

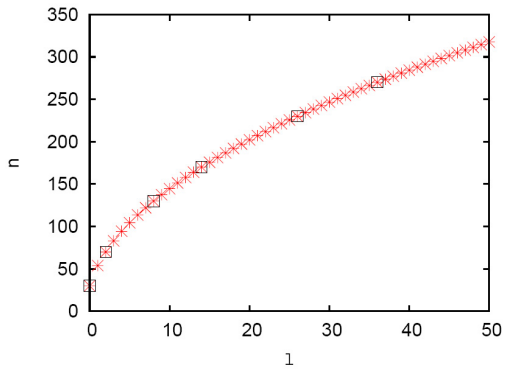

Figure 4.3: Allowed n's for the discretized momentum p_n vs. the Floquet channels l. Each point corresponds to a Floquet channel and each square to an allowed Floquet channel. The parameters are $m = 30$, $\tau = 1$, $L = N\Delta x$ with $\Delta x = \sqrt{2\pi\tau/N}$ and $N = 1000$.

Another important feature, is that the transmission and reflection coefficients can be calculated using the Floquet channels. This could be done by Fourier transforming the incoming and outgoing wave packets in the asymptotic regions, and then, calculating the transmission probability for each channel by means of

$$T(E_l, E) = \left| \frac{p_0}{p_l} \frac{\psi(p_l, t \to \infty)}{\psi(p_0, t \to -\infty)} \right|^2, \tag{4.37}$$

where E is the energy of the incident wave packet and $E_l = E + l\hbar\omega$ is the energy of the transmitted sub-wave-packet. In Fig. 4.4, we plot the incoming and outgoing wave packets in momentum and position representation (insets).

Applying Eq. (4.37) to every allowed Floquet channel, the total transmission probability is finally given by

$$T = \sum_{l=0}^{\infty} T(E_l, E) = \sum_{n=0}^{\infty} \left| \frac{p_0}{p_l} \frac{\psi(p_l, t \to \infty)}{\psi(p_0, t \to -\infty)} \right|^2 \approx 1. \tag{4.38}$$

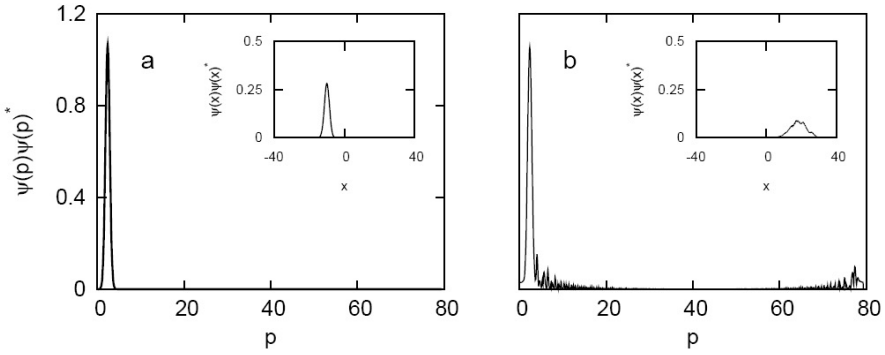

Figure 4.4: Incoming (panel a) and outgoing (panel b) wave packets in momentum and position representation (insets), for an incoming spin up described by the initial Gaussian wave–packet (4.34). The parameters are the same as in Fig. 4.3. The initial conditions are $x_0 = -10$, $A = 1$, $p_0 = 5$ and $a = 4$.

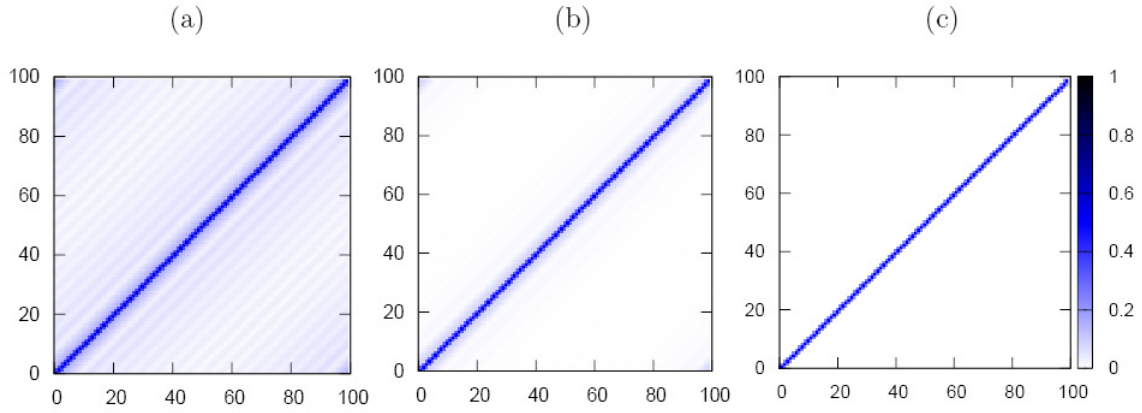

Figure 4.5: Plots of the evolution operator in position representation with parameters, $N = 100$, $a = 4$, $x_0 = -10$ and $\tau = 0.6, A = 10$ (panel a) $\tau = 1, A = 1$ (panel b) $\tau = 1, A = 0$ (panel c). The palette represents the transition probability

To end this section, finally we present the plots of the evolution operator in momentum representation in Fig. 4.5. Analogously to the transmission/reflection plots of the classical case, Figs. 2.10-2.11, from a qualitative point of view, such plots give us information about the possibility to get directed transport. Due to the fact that $\langle p|U|p'\rangle$ can be understood as the probability amplitude of a particle with momentum p' to evolve into the momentum p and the transpose $\langle p'|U|p\rangle$ can be interpreted as the probability amplitude of a particle with momentum p to evolve into the momentum p', the symmetry respect to the diagonal, can be interpreted as an equal transition probability in momentum. In other words, a null directed current, which is the expected result mainly due to the remaining spatial symmetry.

4.3 The Floquet Operator for Coupled Spinors

Now, we consider the case of two perpendicular magnetic fields. If the magnetic field have two-components, the separation of the Schrödinger equations for ψ_+ and ψ_- (4.32-4.33) no longer applies. The Hamiltonian for such a system is given by

$$H(x,t) = I\frac{\hat{p}^2}{2m_0} - \mu_B \hat{\sigma}\cdot\vec{B}(x,t), \tag{4.39}$$

where we choose the magnetic field as $\vec{B}(x,t) = (0, B_y, B_z)$, with

$$B_y = A_y f(x-a/2)\sum_{n=-\infty}^{\infty}\delta(n\tau - t), \quad B_z = A_z f(x+a/2)\sum_{n=-\infty}^{\infty}\delta(n\tau - t)\,, \tag{4.40}$$

and $f(x)$ given by the envelope function Eq. (4.23). In this case, the stroboscopic picture of the evolution of the quantum system can be expressed as in (4.9), with the free evolution operator given by

$$\hat{U}_{\text{free}} = \exp\left(-\frac{i}{\hbar}\hat{H}_0\tau\right) = \exp\left(-\frac{i}{\hbar}\hat{I}H_0\tau\right), \tag{4.41}$$

where $\hat{I}$ is the identity matrix. Using the relation

$$\exp(i\alpha\hat{I}) \;=\; \sum_{n=0}^{\infty}\frac{(i\alpha\hat{I})^n}{n!} = \hat{I}\sum_{n=0}^{\infty}\frac{(i\alpha)^n}{n!} = \hat{I}\exp(i\alpha), \tag{4.42}$$

we could rewrite the expression (4.41) in matrix form

$$\hat{U}_{\text{free}} = \hat{I}\exp\left(-\frac{i}{\hbar}H_0\tau\right) = \begin{pmatrix} U_{\text{free}} & 0 \\ 0 & U_{\text{free}}\end{pmatrix}. \tag{4.43}$$

On the other hand, the kick operator can be written as

$$\hat{U}_{\text{kick}} \;=\; \exp\left(-\frac{i}{\hbar}\hat{V}\right) = \exp\left(\frac{i}{\hbar}\mu_B\hat{\sigma}_y B_y\right)\exp\left(\frac{i}{\hbar}\mu_B\hat{\sigma}_z B_z\right), \tag{4.44}$$

by using the relation

$$\begin{aligned}
\exp(i\alpha_k\hat{\sigma}_k) \;&=\; \sum_{n=0}^{\infty}\frac{(i\alpha_k\hat{\sigma}_k)^n}{n!} = \sum_{n=0}^{\infty}\frac{(i\alpha_k\hat{\sigma}_k)^{2n}}{2n!} + \sum_{n=0}^{\infty}\frac{(i\alpha_k\hat{\sigma}_k)^{2n+1}}{(2n+1)!} \\
&=\; \sum_{n=0}^{\infty}\frac{i^{2n}\alpha_k^{2n}\hat{\sigma}_k^{2n}}{2n!} + \sum_{n=0}^{\infty}\frac{i^{2n+1}\alpha_k^{2n+1}\hat{\sigma}_k^{2n+1}}{(2n+1)!} \\
&=\; \hat{I}\sum_{n=0}^{\infty}\frac{(-1)^n\alpha_k^{2n}}{2n!} + i\hat{\sigma}_k\sum_{n=0}^{\infty}\frac{(-1)^n\alpha_k^{2n+1}}{(2n+1)!}\,,
\end{aligned}$$

we get

$$\exp(i\alpha_k\hat{\sigma}_k) \;=\; \hat{I}\cos\alpha_k + i\hat{\sigma}_k\sin\alpha_k. \tag{4.45}$$

In matrix form

$$U_{\text{kick}} \;=\; \exp\left(-\frac{i}{\hbar}\hat{V}\right) = \begin{pmatrix} U_{11} & U_{12} \\ U_{21} & U_{22} \end{pmatrix}, \tag{4.46}$$

with

$$\begin{aligned} U_{11} &= \cos\left(\frac{\mu_B B_y}{\hbar}\right)\exp\left(i\frac{\mu_B B_z}{\hbar}\right), \\ U_{12} &= \sin\left(\frac{\mu_B B_y}{\hbar}\right)\exp\left(-i\frac{\mu_B B_z}{\hbar}\right), \\ U_{21} &= -\sin\left(\frac{\mu_B B_y}{\hbar}\right)\exp\left(i\frac{\mu_B B_z}{\hbar}\right), \\ U_{22} &= \cos\left(\frac{\mu_B B_y}{\hbar}\right)\exp\left(-i\frac{\mu_B B_z}{\hbar}\right). \end{aligned} \tag{4.47}$$

With the previous results, the time evolution over one period of the driving, could be written as

$$\begin{pmatrix} \psi_+ \\ \psi_- \end{pmatrix}^{n+1} = \begin{pmatrix} U_{\text{free}} & 0 \\ 0 & U_{\text{free}} \end{pmatrix}\begin{pmatrix} U_{11} & U_{12} \\ U_{21} & U_{22} \end{pmatrix}\begin{pmatrix} \psi_+ \\ \psi_- \end{pmatrix}^{n} \tag{4.48}$$

In order to write the states in position representation, we must write also the matrix U_{kick} in the same representation. The easiest way to do such discretisation, is breaking the whole numerical regions into every kind of interaction (See Fig. 4.6).

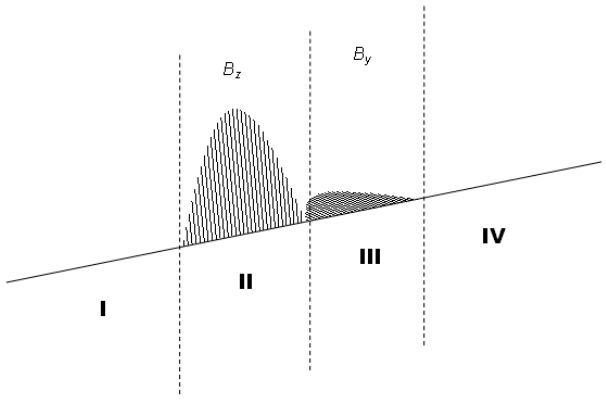

Figure 4.6: Graphics of the different kinds of interaction in the whole numerical region.

With this in mind, the matrix for the kicks in position representation is given by

$$U_{\text{kick}} = \begin{pmatrix} \text{I} & \text{II} & \text{III} & \text{IV} & \text{I} & \text{II} & \text{III} & \text{IV} \\ I & 0 & 0 & 0 & 0 & 0 & 0 & 0 \\ 0 & U_{11} & 0 & 0 & 0 & 0 & 0 & 0 \\ 0 & 0 & U_{11} & 0 & 0 & 0 & U_{12} & 0 \\ 0 & 0 & 0 & I & 0 & 0 & 0 & 0 \\ 0 & 0 & 0 & 0 & I & 0 & 0 & 0 \\ 0 & 0 & 0 & 0 & 0 & U_{22} & 0 & 0 \\ 0 & 0 & U_{21} & 0 & 0 & 0 & U_{22} & 0 \\ 0 & 0 & 0 & 0 & 0 & 0 & 0 & I \end{pmatrix}, \tag{4.49}$$

and the states are written as column vectors of the form

$$\psi = (\psi_+^1, \ldots, \psi_+^n, \psi_-^1, \ldots, \psi_-^n). \tag{4.50}$$

Here the superscript is related to space instead of time as was used in the previous notation.

4.3.1 Directed Transport

From the relation for the time evolution over one period for spinors (4.48), we could get information about the behavior of the initial states. If we assume the first field B_z to be parallel to the initial state, the dynamical behavior in the first region, is analog to the quantum mechanical problem of a particle in the presence of a potential well (barrier) for spins up (down), as we show in section 4.2.

The interaction with the second field B_y is given by a 2-dimensional rotation matrix, it means that the effect of the second field is to induce in the neutral particle precessions around the y-axis. Given an initial spin-up state, the presence of the second magnetic field introduces the possibility to obtain an outgoing spin-down state after the scattering process (see e.g. Fig. 4.7).

In what follows, we have included the plots of the evolution operator in momentum representation, that are of a more general nature signs about the possibility to get directed transport. As was explained in the previous section, from a qualitative point of view, such plots give us information about the transition probability in momentum, which means a null directed current in the case of symmetry respect to the diagonal. As can be seen in Fig. 4.8, the only asymmetric configuration of momentum distribution is the one which breaks the spatial symmetry (panel a). The case of equal amplitudes in the magnetic field (panel b), give us a symmetric plot which must be related to a zero current. Finally the case of a free particle (panel c), show us that the transition probability to a momentum different of the incoming one is zero.

In Fig. 4.9 we first show the comparison between particle and spin current as a function of the angular frequency for a fixed amplitude of the fields (panel a). The data presented in

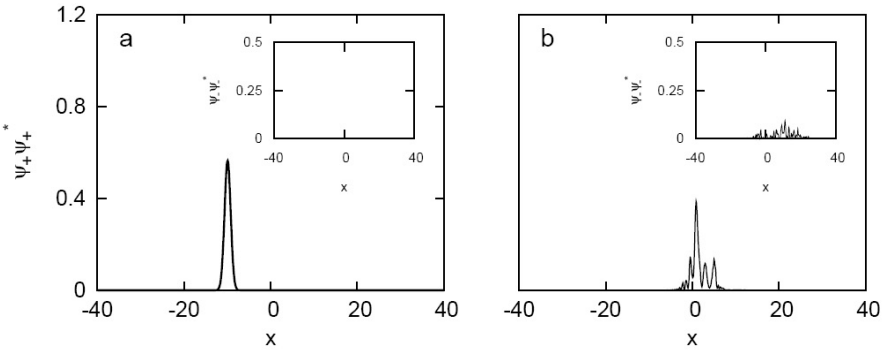

Figure 4.7: Time-evolution of the probability density for an initial spin-up state in position representation (4.34) at times $t = 0$ (panel a) and $t = 2.5$ (panel b). The simultaneous evolution of the probability density for the spin-down state is shown in the insets. The initial conditions are $x_0 = -10$, $A_y = 1, A_z = 8$, $p_0 = 5$ and $a = 4$.

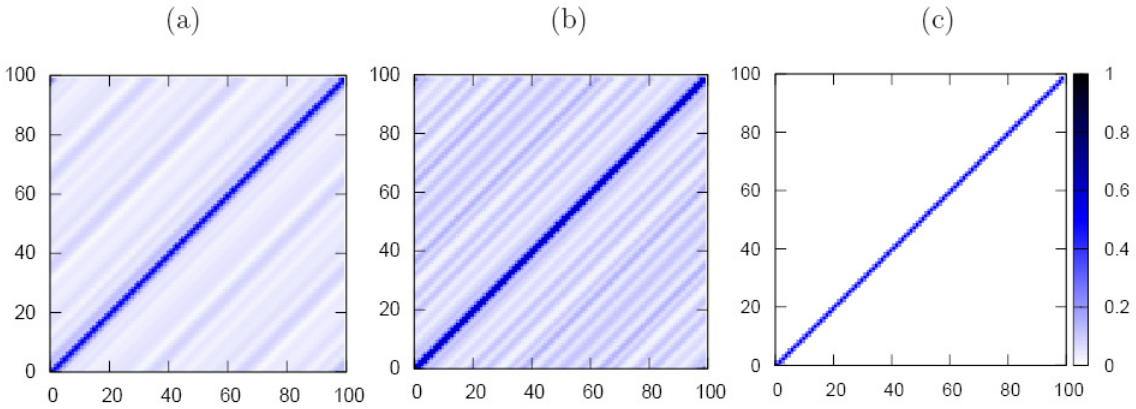

Figure 4.8: Plots of the evolution operator in position representation with parameters, $N = 100$, $a = 4$ and $\tau = 0.6, A_z = 1, A_y = 100$ (panel a) $\tau = 1, A_z = A_y = 100$ (panel b) $\tau = 1, A_z = A_y = 0$ (panel c). The palette represents the transition probability

Fig 4.9 indicate the existence of polarized currents for certain regions of the parameter space. As we sketch in Fig. 2.13, also here we find zeros of the particle current I_{p} at appreciable values of the spin current I_{s}, giving rise to a pure spin current. The presence or absence of the symmetry is clearly reflected in the transport features, as can be seen in Fig. 4.9 (panel b), where we plot the comparison between particle and spin current as a function of the amplitude of the field B_z. In the same figure can be seen that there is a tendency to a saturation in both of the currents. This is an important result from the practical point of view, where there exist an experimental limit on the strength of the field. However, we emphasize that when very high strengths of the field are considered, the pure spin currents do not appear any more.

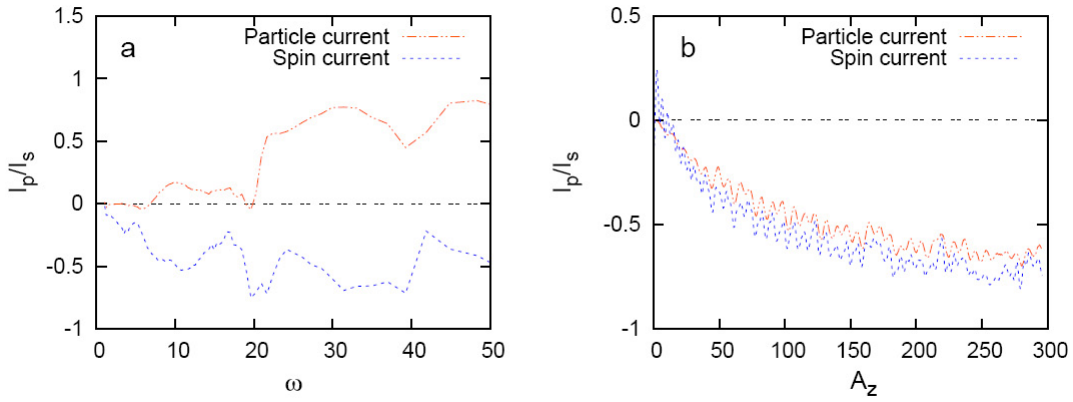

Figure 4.9: Comparison of particle current $I_{\rm p}$ (red curve) to spin current $I_{\rm s}$ (blue curve), averaged over the initial phase $\varphi_{\rm in}$, as functions of the driving frequency ω (panel a) and the magnetic field strength A_z (panel b). Parameters are $A_z = 1$, $A_y = 10$, $a = 4$, $p_0 = 5, x_0 = -10$ (panel a) and $A_y = 1, a = 4, p_0 = 5, x_0 = -10, \tau = 1.6$ (panel b). In panel b, we may see that the current vanishes for the partial recovery of spatial symmetry, $A_y = A_z = 1$.

4.4 Summary

In this chapter we demonstrate that the quantum stroboscopic evolution of an initial Gaussian state, in the presence of a single-component kicked magnetic field, is analog to the quantum mechanical problem of a particle in the presence of a potential well for an incoming spin up, or a potential barrier for an incoming spin down. The multiphoton absorption/emission process, allows us to calculate the transmission and reflection probabilities, and therefore, the particle and spin currents in terms of the Floquet channels. Through the quantization of the classical model with two perpendicular magnetic fields, we have showed that the basic mechanism responsible for the separation of spins in the classical case, carries over to the quantum level, giving rise to a spin pump capable of generating polarized spin currents. The transport of mass and spin we observe, takes place only by breaking the spatio-temporal symmetries and do not require a two-parameter driving as in adiabatic pumping. Yet, we underline that in the adiabatic limit, the particle and spin current diminish significatively, and hence, the pure spin currents also disappear. Finally, we find that the spin current is sensitive to the strength of the magnetic field and to the driving frequency, so from an experimental point of view, we can conveniently control the pumped spin current by tuning the field strength and/or the period of the driving. The last statement should be taken carefully, because despite the particle current as well as the spin current increases while the field strength increases, for very high strengths of the field the pure spin currents vanish. A work along this line will be soon published [45].

5 Conclusions

With this work we intend to demonstrate the feasibility of pumping spin in a quantum system whose classical counterpart exhibit chaotic dynamics. As a preparatory survey aiming towards chaotic spin pumping, first, we took in to account the classical version of the system. We have shown that is possible to pump angular momentum in the regime of fast and strong driving, where adiabatic or perturbative methods would fail. The transport phenomena we observe, both of mass and angular momentum, owe themselves to an interplay of strongly nonlinear dynamics and the breaking of spatio-temporal symmetries. On the one hand, they go far beyond the frame of linear response, while on the other, they do not require a two-parameter driving, just an asymmetric profile of the external force.

Our classical results constitute an important example of how an internal degree of freedom not only participates in chaotic scattering, but even gives rise to new phenomena. While in this thesis we focus on transport, the aspect of chaotic scattering with internal freedoms deserves a closer scrutiny in a separate effort. Another relevant side issue is the fact that spin separation clearly corresponds to a reduction of entropy. As we here remain within a perfectly deterministic Hamiltonian setup, a more realistic model including thermodynamic aspects however would urgently have to address this question.

A detailed description of a phenomenon in terms of the underlying nature of the system was desirable to study the quantum version of the system. This was done by means of quantum dynamics simulations. More specifically, we have described a numerical integration method for the time–dependent Schrödinger equation with an without source terms. The numerical integration was done using the Crank-Nicholson method together with a Cayley's form for the finite-difference representation of evolution operator which produces an stable, unitary, and second-order accurate in space and time method. On replacing the Hamiltonian by its finite-difference approximation in position, we have reduced the problem to a complex tridiagonal system. As the most important result concerning the numerical artifacts, we have simplified the numerical scheme inverting by hand the evolution matrices by means of the Usmani's formula for Jacobian matrices, which reduces the computational effort drastically.

Finally we have considered a simplified version of the quantum system, where we demonstrate that the quantum stroboscopic evolution of an initial Gaussian state, in the presence

of a single-component kicked magnetic field, is analog to the quantum mechanical problem of a particle in the presence of a potential well for an incoming spin up, or a potential barrier for an incoming spin down. This result shows us that the basic mechanism responsible for the separation of spins in the classical case, carries over to the quantum level. Through the consideration of the general problem with two perpendicular magnetic fields, we have showed that as the classical version, the quantum system is capable of generating polarized spin currents. The transport of mass and spin we observe, takes place only by breaking the spatio-temporal symmetries and do not require a two-parameter driving as in adiabatic spin pumping. We find that the spin current is sensitive to the strength of the magnetic field and to the driving frequency, so from an experimental point of view, we can conveniently control the pumped spin current by tuning the field strength and/or the period of the driving. While here we focus on the transport properties, a more deep study of the classical and quantum correspondence is left for future work.

A

Neutral Particle in an Inhomogeneous Magnetic Field

Must be shown that the motion of a classical particle with mass m_0 and spin $\mathbf{s}$ in the presence of a magnetic field $\mathbf{B}(\mathbf{x})$, is described by the equations

$$m_0\ddot{\mathbf{x}} = \gamma\nabla(\mathbf{B}\cdot\mathbf{s}) \tag{A.1}$$
$$\dot{\mathbf{s}} = \gamma\,\mathbf{s}\times\mathbf{B}. \tag{A.2}$$

The Hamiltonian for the system is given by

$$\mathcal{H} = \frac{\mathbf{p}^2}{2m_0} - \gamma\,\mathbf{B}\cdot\mathbf{s}\,, \tag{A.3}$$

where $\mathbf{p}$ is the canonical conjugate momentum (hereinafter $m_0 = \gamma = 1$).

The vector $\mathbf{s}$ can be decomposed into the cartesian coordinates xyz as

$$\begin{aligned} s_x &= |\mathbf{s}|\sin\theta\cos\varphi, \\ s_y &= |\mathbf{s}|\sin\theta\sin\varphi, \\ s_z &= |\mathbf{s}|\cos\theta, \end{aligned}$$

where θ is the polar angle and φ the azimuth. Denoting $|\mathbf{s}| = s$ and $m = s\cos\theta$, the spin projections are written as

$$s_x = (s^2 - m^2)^{1/2}\cos\varphi, \tag{A.4}$$
$$s_y = (s^2 - m^2)^{1/2}\sin\varphi, \tag{A.5}$$
$$s_z = m. \tag{A.6}$$

The Hamiltonian in terms of the new variables could be written as

$$\mathcal{H}(\mathbf{p},\mathbf{x},\varphi,m) = \frac{\mathbf{p}^2}{2} - [(s^2 - m^2)^{1/2}(B_x\cos\varphi + B_y\sin\varphi) + mB_z].$$

From the Hamilton equations of motion

$$\dot{p}_i = -\frac{\partial \mathcal{H}}{\partial q_i}, \qquad \dot{q}_i = \frac{\partial \mathcal{H}}{\partial p_i}, \tag{A.7}$$

we have

$$\begin{aligned}
\dot{\mathbf{p}} &= -\frac{\partial \mathcal{H}}{\partial \mathbf{x}} = \frac{\partial}{\partial \mathbf{x}} \left[(s^2 - m^2)^{1/2} (B_x \cos\varphi + B_y \sin\varphi) + m B_z \right] , && \text{(A.8)} \\
\dot{\varphi} &= \frac{\partial \mathcal{H}}{\partial m} = m(s^2 - m^2)^{-1/2} (B_x \cos\varphi + B_y \sin\varphi) - B_z \, , && \text{(A.9)} \\
\dot{m} &= -\frac{\partial \mathcal{H}}{\partial \varphi} = (s^2 - m^2)^{1/2} (B_y \cos\varphi - B_x \sin\varphi) \, , && \text{(A.10)} \\
\dot{\mathbf{x}} &= \frac{\partial \mathcal{H}}{\partial \mathbf{p}} = \mathbf{p} \, . && \text{(A.11)}
\end{aligned}$$

and after substituting (A.11) in (A.8) we get

$$\ddot{\mathbf{x}} = \nabla (\mathbf{B} \cdot \mathbf{s}) \, .$$

To show that equations (A.9) and (A.10) are equivalent to equation (A.2), we start by calculating the derivative with respect to time of the equations (A.4-A.6),

$$\begin{aligned}
\dot{s_x} &= -m(s^2 - m^2)^{-1/2} \dot{m} \cos\varphi - \dot{\varphi} (s^2 - m^2)^{1/2} \sin\varphi, \\
\dot{s_y} &= -m(s^2 - m^2)^{-1/2} \dot{m} \sin\varphi + \dot{\varphi} (s^2 - m^2)^{1/2} \cos\varphi, \\
\dot{s_z} &= \dot{m} \, .
\end{aligned}$$

On the other hand, the cross product components in terms of the spin projections are given by

$$\begin{aligned}
(\mathbf{s} \times \mathbf{B})_x &= (s^2 - m^2)^{1/2} \sin\varphi B_z - m \, B_y \, , \\
(\mathbf{s} \times \mathbf{B})_x &= m \, B_x - (s^2 - m^2)^(1/2) \cos\varphi B_z \, , \\
(\mathbf{s} \times \mathbf{B})_z &= (s^2 - m^2)^{1/2} \cos\varphi B_y - (s^2 - m^2)^{1/2} \sin\varphi B_x \, .
\end{aligned}$$

Equating the derivatives and cross products

$$\begin{aligned}
-m(s^2 - m^2)^{-1/2} \dot{m} \cos\varphi - \dot{\varphi} (s^2 - m^2)^{1/2} \sin\varphi &= (s^2 - m^2)^{1/2} \sin\varphi B_z - m \, B_y \, , && \text{(A.12)} \\
-m(s^2 - m^2)^{-1/2} \dot{m} \sin\varphi + \dot{\varphi} (s^2 - m^2)^{1/2} \cos\varphi &= m \, B_x - (s^2 - m^2)^{1/2} \cos\varphi B_z \, , && \text{(A.13)} \\
(s^2 - m^2)^{1/2} \cos\varphi B_y - (s^2 - m^2)^{1/2} \sin\varphi &= B_x \dot{m} \, , && \text{(A.14)}
\end{aligned}$$

multiplying (A.12) by $\sin\varphi$ and (A.13) by $-\cos\varphi$ and adding, the system reduces to

$$\begin{aligned}
\dot{\varphi} &= m(s^2 - m^2)^{-1/2} (B_x \cos\varphi + B_y \sin\varphi) - B_z \, , && \text{(A.15)} \\
\dot{m} &= (s^2 - m^2)^{1/2} (B_y \cos\varphi - B_x \sin\varphi) \, , && \text{(A.16)}
\end{aligned}$$

which are the equations (A.9) and (A.10), respectively. It concludes that the Hamiltonian (A.3) leads to the equations (A.1) and (A.2). In other words, a classical particle with mass m_0 and spin $\mathbf{s}$ in the presence of a magnetic field $\mathbf{B}(\mathbf{x})$, is described by the equations of motion (A.1) and (A.2).

B

Particle Current

In literature, the current is defined as the amount of charge (particles) flowing past a specified point per unit time, i.e. $I = \Delta q/\Delta t$. In one dimension the charge and position satisfies the relation $q = \rho x$, or $\Delta q/\Delta t = \rho \Delta x/\Delta t$, with ρ a uniform charge density. For the case of an ensemble of particles in which every particle could move freely in the positive or negative x-direction, the normalized current must be calculated as an average, then from the previous relations, the current is proportional to the mean velocity. On the other hand, transport is also defined as the mean velocity of an ensemble, thats why usually in literature the calculation of currents is referred to as transport.

However should be noted, that in scattering problems the current does not depends explicitly on the velocity, as we will show in the next lines. Lets consider an incoming initial uniform distribution of particles ρ_{in} and suppose they are distributed in some segment before entering the interaction region, then the initial distribution could be written as

$$\rho_{\text{in}} = \frac{1}{d} = \frac{1}{v_{\text{in}} T} = \frac{\omega}{2\pi v_{\text{in}}} = \frac{f}{v_{\text{in}}}\,,$$

and the corresponding outgoing transmitted and reflected densities are given by

$$\rho_{\text{out,t}} = t\frac{f}{v_{\text{out}}} \qquad \rho_{\text{out,r}} = r\frac{f}{v_{\text{out}}}\,,$$

with t and r transmission and reflection coefficients. From the last expressions we may calculate the currents as

$$I_{\text{out,t}} = \rho_{\text{out,t}} v_{\text{out}} = t \times f \quad \text{and} \quad I_{\text{out,r}} = \rho_{\text{out,r}} v_{\text{out}} = r \times f\,,$$

which are independent on the velocities.

The previous argument, lets us define the particle current as the number of particles leaving the scattering region to the right minus the number of particles leaving the scattering region to the left, sending an identical ensemble from the left and right. Denoting T_{lr} the total number of particles transmitted from left to right, R_{ll} the total number of particles

reflected from left to left, T_{rl} the total number of particles transmitted from right to left and R_{rr} the total number of particles reflected from right to right, the current is explicitly given by,

$$I = T_{\mathrm{lr}} + R_{\mathrm{rr}} - R_{\mathrm{ll}} - T_{\mathrm{rl}}\,.$$

In some cases is possible to extract information about the currents form the transmission reflection plots. From the current definition, a null current takes place if,

$$T_{\mathrm{lr}} + R_{\mathrm{rr}} = R_{\mathrm{ll}} + T_{\mathrm{rl}}\,. \tag{B.1}$$

Taking into account that the total number of particles N entering from the left equals the number of particles entering from the right and furthermore, assuming that each particle leaves the interaction region after some time, the coefficients must satisfy

$$T_{\mathrm{lr}} + R_{\mathrm{ll}} = N = T_{\mathrm{rl}} + R_{\mathrm{rr}}\,. \tag{B.2}$$

Getting T_{lr} in (B.2) by itself and replacing it in to (B.1) we find,

$$R_{\mathrm{rr}} = R_{\mathrm{ll}} \qquad \text{and} \qquad T_{\mathrm{rl}} = T_{\mathrm{lr}}\,.$$

Such result tell us that if the reflection and transmission plots looks symmetrical with respect to the incoming direction, the net current should be zero or at least approximately zero.

C

Spin Current

In the particular situation where the spin (or its projection on any direction) is conserved, the spin current is defined as the difference between the streams of particles in the two spin states. In the present case, we consider classical particles with classical magnetic moments associated whose magnitudes are constants, i.e. the spin projection is not quantized nor conserved. To redefine the spin current for the classical case, let us consider the injection of N particles with polar angle θ (measured with respect to the field direction) in the interval $[0, \pi]$ from the left and another N particles with same characteristics from the right. Defining

- $I_{\uparrow}^{+}$ Spin up current leaving the scattering region from the right,
- $I_{\uparrow}^{-}$ Spin up current leaving the scattering region from the left,
- $I_{\downarrow}^{+}$ Spin down current leaving the scattering region from the right,
- $I_{\downarrow}^{-}$ Spin down current leaving the scattering region from the left,

where the spin up and down currents are given respectively by:

$$I_{\uparrow} = I_{\uparrow}^{+} - I_{\uparrow}^{-}\,, \qquad I_{\downarrow} = I_{\downarrow}^{-} - I_{\downarrow}^{+}\,.$$

Now to calculate the expression for the current we explicitly write each of the terms defined above:

$$\begin{aligned}
I_{\uparrow}^{+} &= \sum^{+} \cos\theta_{\mathrm{lr}} + \sum^{+} \cos\theta_{\mathrm{rr}}, \\
I_{\uparrow}^{-} &= \sum^{+} \cos\theta_{\mathrm{ll}} + \sum^{+} \cos\theta_{\mathrm{rl}}, \\
I_{\downarrow}^{+} &= \sum^{-} \cos\theta_{\mathrm{lr}} + \sum^{-} \cos\theta_{\mathrm{rr}}, \\
I_{\downarrow}^{-} &= \sum^{-} \cos\theta_{\mathrm{ll}} + \sum^{-} \cos\theta_{\mathrm{rl}},
\end{aligned}$$

where $\theta_{\alpha\beta}$ denotes the measured angle after the scattering process for a particle entering for α and leaving for β with $l \rightarrow$ left and $r \rightarrow$ right. The sign "+" ("-") over the sum denotes a sum of positive (negative) numbers.

The spin current $I_s = I_\uparrow - I_\downarrow$, in terms of the polar angles could be written as

$$\begin{aligned} I_s &= \left(\sum^{+} \cos\theta_{\rm lr} + \sum^{-} \cos\theta_{\rm lr}\right) - \left(\sum^{+} \cos\theta_{\rm ll} + \sum^{-} \cos\theta_{\rm ll}\right) \\ &+ \left(\sum^{+} \cos\theta_{\rm rr} + \sum^{-} \cos\theta_{\rm rr}\right) - \left(\sum^{+} \cos\theta_{\rm rl} + \sum^{-} \cos\theta_{\rm rl}\right), \end{aligned}$$

or in other words,

$$I_s = \frac{1}{N}\left(\sum \cos\theta_{\rm lr} + \sum \cos\theta_{\rm rr} - \sum \cos\theta_{\rm ll} - \sum \cos\theta_{\rm rl}\right).$$

Here, the normalization has been done dividing the sum by N as this is the maximum value that all spins could achieve if they were completely aligned with the field after the scattering process.

Bibliography

[1] G. A. Prinz, *Science*, **282**, 1660 (1998).

[2] M. Scheid, A. Pfund, D. Bercioux, K. Richter *Phys. Rev. B* **76**, 195303 (2007).

[3] W. Zheng, J. Wu, B. Wang, J. Wang, Q. Sun, and H. Guo, *Phys. Rev. B* **68**, 113306 (2003).

[4] P. K. Papachristou, F. K. Diakonos, V. Constantoudis, P. Schmelcher, and L. Benet, *Phys. Rev. E*, **70**, 056215 (2004).

[5] E.R. Mucciolo, C. Chamon, C.M. Marcus, *Phys. Rev. Lett.*, **89**, 146802 (2002) .

[6] H.-D. Meyer, U. Manthe and L.S. Cederbaum, *Chem. Phys. Lett.*, **165** (1), 73 (1990).

[7] M. Henseler, T. Dittrich, and K. Richter, *Europhys. Lett.*, **49**, 289 (2000).

[8] M. Henseler, T. Dittrich, and K. Richter, *Phys. Rev. E*, **64**, 046218 (2001).

[9] R. G. Littlejohn and S. Weigert, *Phys. Rev. A*, **924**, 48 (1993).

[10] S. Garzón, *Scattering irregular de un spin en un campo magnético gaussiano* MSc thesis (Bogota: Universidad de los Andes). (1999).

[11] U. Smilansky and R. Blümel, *Phys. Blätter*, **45**, 379 (1989).

[12] S. Flach, O. Yevtushenko, and Y. Zolotaryuk, *Phys. Rev. Lett.*, **84**, 2358 (2000).

[13] T. Dittrich, R. Ketzmerick, M. F.Otto, and H. Schanz, *Ann. Phys.* (Leipzig), **9**, 755 (2000).

[14] H. Schanz, T. Dittrich, R. Ketzmerick and M. F.Otto, *Phys. Rev. Lett.*, **87**, 070601 (2001).

[15] H. Schanz, T. Dittrich and R. Ketzmerick, *Phys. Rev. E*, **71**, 26228 (2005).

[16] T. Dittrich, M. Gutiérrez, and G. Sinuco, *Physica A*, **327** 145 (2003).

[17] D. J. Thouless, *Phys. Rev. B*, **27**, 6083 (1983).

[18] P. W. Brouwer, *Phys. Rev. B*, **58**, R10135 (1998).

[19] B. L. Altshuler and L. I. Glazman, *Science*, **283**, 1864 (1999).

[20] M. Jääskeläinen, C. Corvino, C. P. Search, and V. Fessatidis, *Phys. Rev. B*, **77**, 155319 (2008).

[21] M. Scheid, M. Wimmer, D. Bercioux, and K. Richter, *Phys. Stat. Sol.*, **3**, 4235 (2006).

[22] M. Scheid,A. Pfund, D. Bercioux, and K. Richter, *Phys. Rev. B*, **76**, 195303 (2007).

[23] M. Scheid, D. Bercioux, and K. Richter, *N. J. Phys.*, **9**, 401 (2007).

[24] F. L. Dubeibe and T. Dittrich *Rev. Col. Fís.*, **42** 2 (2009).

[25] F. L. Dubeibe and T. Dittrich, *J. Phys. A: Math. Theor.*, **41** 265102 (2008).

[26] D. Culcer, J. Sinova, N.A. Sinitsyn, T. Jungwirth, A. H. MacDonald, and Q. Niu, *Phys. Rev. Lett.*, **93**, 046602 (2004).

[27] W. Kim, R. K. Teshima, and F. Marsiglio, *Europhys. Lett.*, **69**, 595 (2005).

[28] E. J. Heller, K. E. Aidala, B. J. LeRoy, A.C. Bleszynski, A. Kalben, R. M. Westervelt, K. D. Maranowski, and A. C. Gossard, *Nano Lett.*, **5**, 1285 (2005).

[29] K. LeHur, *Phys. Rev. B*, **74**, 165104 (2006).

[30] A. Tornberg and B. Engquist, *Journal of computational physics*, **200** (2), 462 (2004).

[31] T. Paul, M. Hartung, K. Richter and P. Schlagheck, *Phys. Rev. A.*, **76**, 063605 (2007).

[32] R. Usmani, *Linear Algebra Appl.*, **212** 413 (1994).

[33] F. Dubeibe, submmited to *Am. J. Phys.* (2010).

[34] T. Dittrich, P. Hänggi, G. Ingold, B. Kramer, G. Schön and W. Zwerger *Quantum Transport and Dissipation* (Wiley: Weinheim, 1998) chap 5.

[35] U. Smilansky, *Les Houches Lectures XXXVI*, Iooss G, Helleman R H G, and Stora R (eds.) (Amsterdam: North Holland, 1981).

[36] E. Ott, *Chaos* **3** 4 (1993).

[37] E. Ott, *Chaos in dynamical systems* (Cambridge: Cambridge University Press, 1993) Chap 5.5.

[38] P. Šeba, *Phys. Rev. E.*, **47** (6), 3870 (1992).

[39] P. Šeba, *Phys. Rev. E.*, **50** (5), 3615 (1994).

[40] W. H. Press, S. A. Teukolsky, W. T. Vetterling, and B. P. Flanery *Numerical Recipes in C++* (Cambridge University Press, Cambridge, 2002).

[41] W. A. Ames, *Numerical Methods for Partial Differential Equations* (Academic, New York, 1977).

[42] S. M. Blinder, *Am. J. Phys.* **36(6)** 525 (1968).

[43] T. Shibata, *Phys. Rev. B.* **43** 6760 (1991).

[44] F. Haake. *Quantum signatures of chaos* (Springer-Verlag, Berlin, 2nd edition, 1991).

[45] F. L. Dubeibe and T. Dittrich, to be submmited to *Europhys. Lett.* (2010).